Revision 2

Mineralogy and bulk geochemistry of a fumarole at Hverir, Iceland: Analog for acid-sulfate leaching on Mars

Word count: 15,114

George L. Carson[1,+]
Lindsay J. McHenry[1,*]
Brian M. Hynek[2]
Barry I. Cameron[1]
Chase T. Glenister[1]

* corresponding author

1. Department of Geosciences, University of Wisconsin- Milwaukee. 3209 N. Maryland Ave., Milwaukee, WI 53211. lmchenry@uwm.edu. Phone: 414 229-3951. Fax: 414 229-5452.
2. Laboratory for Atmospheric and Space Physics, University of Colorado Boulder, 1234 Innovation Drive, Boulder, CO 80303
+ Present address: 610 Winona Ct APT 28, Denver, CO 80204

Key words: Hydrothermal alteration; Mars analog; sulfate mineralogy

Abstract

Iceland's Námafjall geothermal area exhibits a range of alteration environments. Geochemical and mineralogical analyses of fumaroles and hot springs interacting with Holocene basaltic lavas at Hverir, and with Pleistocene hyaloclastites atop nearby Námaskarð, reveal different patterns of alteration depending on water-rock ratio, degree of oxidation, and substrate composition and age. The focus of this study is a transect of a Hverir fumarole that has formed a bulls-eye pattern of alteration of a Holocene basaltic lava flow. Surface samples and samples collected from shallow pits were analyzed by X-ray Diffraction (XRD), X-ray Fluorescence (XRF), and Scanning Electron Microscopy (SEM) to constrain changes in mineral assemblage and major elemental composition with both distance and depth. Elemental sulfur is concentrated near the vent, with leached deposits with amorphous silica and anatase nearby and kaolinite, hematite, and jarosite/alunite-group sulfate minerals farther out, with smectites and less altered material at the margins, though smaller-scale mineralogical diversity complicates this pattern.

Silica phases include amorphous silica (most samples), cristobalite (some samples, in the leached part of the apron), and quartz (minor constituent of few samples). The silica was concentrated through residual enrichment caused by leaching, and is accompanied by a significant enrichment in TiO_2 (in anatase). The presence of abundant cristobalite in a surface fumarole-altered Holocene basaltic lava flow most likely reflects cristobalite formed during the devitrification of volcanic glass or precipitation from fumarolic vapors, rather than high-temperature processes. Minor, localized quartz likely reflects diagenetic maturation of earlier-formed amorphous silica, under surface hydrothermal conditions. Natroalunite, natrojarosite, and jarosite are all present

and even exhibit compositional zonation within individual crystals, showing that under surface hydrothermal conditions, these minerals can form a significant solid solution.

The high iron content of the substrate basalt and the prevalence of Fe-sulfates and Fe-oxide spherules among the alteration products makes this geothermal area an especially useful analog for potential Martian hydrothermal environments. The residual enrichment of silica in the leached deposits of the Hverir fumarole apron could serve as an acid-sulfate leaching model in which amorphous silica forms without appreciable sulfur-bearing phases in many samples, a possible analog for silica-rich soils in the Columbia Hills on Mars. The co-existence of hematite spherules and jarosite-group minerals serves as an intriguing analog for a volcanic/hydrothermal model for hematite and jarosite occurrences at Meridiani Planum.

Introduction

Volcanic hydrothermal deposits are key targets for astrobiological research, since they can provide warm, wet environments on or below otherwise inhospitably cold planetary surfaces, and since terrestrial examples provide a habitat for a variety of extremophile microorganisms. The characterization of likely hydrothermal deposits in the Columbia Hills explored by the Mars Exploration Rover (MER) Spirit (e.g., Yen et al., 2008), and the detection of likely hydrothermal deposits from orbit by the Mars Reconnaissance Orbiter (MRO, e.g. Skok et al., 2010), have made understanding the astrobiological potential of these environments a priority for NASA's Mars exploration program.

Iceland provides an excellent analog for potential Martian hydrothermal sites because of the wide variety of hydrothermal environments coupled with their interaction with high-iron basalts comparable to those found on Mars. This study describes an analog site in northeastern Iceland (Hverir), where acid-sulfate fumaroles interact with relatively young basaltic lavas, forming alteration and precipitated products representing a range of temperature and redox conditions. The redox gradients observed in these deposits could provide an energy source for iron or sulfur reducing or oxidizing microbes.

The objectives of this work were to (1) characterize the mineral assemblages and major element distribution for altered and precipitated samples at the surface and at shallow depth at increasing distances from an active fumarole at Hverir, (2) conceptually model the processes of leaching and mineral precipitation in terms of changing pH, oxidation, and temperature conditions, and (3) consider these trends in the context of Mars hydrothermal deposits.

Background

Mars Hydrothermal Activity

A long, early history of basaltic volcanism, plus mineralogical and geomorphological evidence for surface water in the ancient rock record, suggest that volcanic hydrothermal activity likely occurred on early Mars. Hydrothermal environments on Mars could provide sources of

heat, energy, and water for life (Walter & Des Marais, 1993; Schulze-Markuch et al., 2007; Hynek et al., 2013, 2018), even when it is too dry or cold for life to persist nearby. A hydrothermal origin has been proposed for some Mars surface features, including the mineralogy and geochemistry of some outcrops and soils studied by Mars Exploration Rover (MER) Spirit in the Columbia Hills (e.g. Yen et al., 2008), and potential hydrothermal mineral assemblages identified from orbit (e.g. Ehlmann et al., 2009, 2011; Skok et al., 2010). The Observatoire pour la Minéralogie, l'Eau, les Glaces et l'Activité (OMEGA) instrument aboard Mars Express, the Compact Reconnaissance Imaging Spectrometer for Mars (CRISM) aboard the MRO, the MER missions, and the Mars Science Laboratory (MSL) Curiosity rover have identified globally distributed mono- and poly-hydrated Mg/Ca/Fe-sulfates within diverse geologic settings that include sedimentary and hydrothermal environments (Langevin et al., 2005; Yen et al., 2008; Nachon et al., 2014*)*. MER Opportunity and Spirit, along with MSL Curiosity, detected iron oxides and oxyhydroxides that include hematite and goethite (Klingelhöfer et al., 2004; Morris et al., 2008; Fraeman et al., 2016). Chojnacki and Hynek (2008) attribute some of the widespread Valles Marineris sulfate deposits to high temperature basalt alteration, and widespread jarosite-bearing deposits at Syrtis Major could also have been formed hydrothermally (Ehlmann and Mustard, 2012; Ehlmann and Edwards, 2014). Potential products of Martian hydrothermal alteration have also been identified in Martian meteorites, particularly nakhlites (e.g. Bridges and Schwenzer, 2012). Schulze-Makuch et al. (2007) outline targets for Martian hydrothermal environments, and researchers have proposed hydrothermal activity as a possible explanation for certain mineralogical features of both Mawrth Vallis (Bishop et al., 2008) and Nili Fossae (Ehlmann et al., 2009; Viviano et al., 2013), perennial favorites for future landed missions. Gale crater, the MSL landing site currently under investigation by Curiosity, has abundant sulfates and

116 phyllosilicates (Milliken et al., 2010), likely formed in part by basalt alteration, and Mangold et
117 al. (2012) have even suggested a hydrothermal origin for some of its deposits. This interpretation
118 is bolstered by the discovery of the high-temperature SiO_2 polymorph mineral tridymite (Morris
119 et al., 2016) and disordered adularia and specular hematite (Morris et al., 2020, Rampe et al.,
120 2020) in the Gale crater sediments. Finally, Martian impact craters represent another class of
121 features that likely hosted long-lived hydrothermal systems (e.g., Abramov and Kring, 2005;
122 Osinski et al., 2013; Schwenzer and Kring, 2013).
123
124 In the Columbia Hills, the Spirit rover analyzed soils and outcrops and identified both
125 mineralogical and geochemical patterns consistent with hydrothermal alteration of basalts. The
126 Paso Robles class soils are sulfate-rich, with Ca, Mg, and ferric sulfates, along with amorphous
127 silica and hematite; in the case of Paso Robles and Arad these have been interpreted as likely
128 fumarolic deposits with lower water/rock ratios, while at the Tyrone locality conditions were
129 likely wetter (Wang et al., 2008; Yen et al., 2008; Schmidt et al., 2008; 2009; Hausrath et al.,
130 2013). Deposits rich in amorphous silica (Opal-A) in the Eastern Valley have been variously
131 attributed to hydrothermal acid-sulfate leaching (e.g. Squyres et al., 2008; Morris et al., 2008) or
132 sinter precipitation in a near-neutral hot spring environment (e.g. Ruff et al., 2011; Ruff and
133 Farmer, 2016), though morphological and stratigraphic considerations favor the latter (Ruff et
134 al., 2020). Reconciling these different hydrothermal interpretations is critical for assessing
135 potential habitability.
136
137 Hematite (as spherules) and sulfates (including jarosite) are also abundant in the Burns
138 Formation, investigated by the MER Opportunity rover at Meridiani Planum. While most often

interpreted as a sedimentary deposit (hematite precipitated as nodules in the subsurface by the action of groundwater, sulfates produced through evaporitic processes), a volcanic or hydrothermal origin has also been suggested (McCollom and Hynek, 2005, 2006, 2021). The presence of jarosite in particular, as identified based on Mössbauer spectroscopy, has been used to argue for overall acidic and oxidizing conditions, given the limited stability field of jarosite. Some studies have questioned this interpretation, based on the presence of jarosite in non-acidic environments on Earth (e.g. saline-alkaline paleolake Olduvai, Tanzania: McHenry et al., 2011) and concerns about the ability of Mössbauer to unambiguously distinguish between jarosite and iron-bearing natroalunite, which has a less restrictive stability field (McCollom et al., 2013b).

Iceland

The Krafla central volcano in northern Iceland lies above the Icelandic mantle plume at the Mid-Atlantic Ridge within the Northern Volcanic Zone. Krafla volcano forms a low, broad shield (~25 km diameter); with an 8 by 10 km caldera bisected by a 100 km en echelon NNE-trending fissure swarm (Figure 1a) (Gudmundsson & Arnorsson, 2002, 2005). The Krafla central volcano exhibits a distinct dacitic welded-tuff caldera rim that formed ~110 ka ago (Björnsson et al., 1977). The caldera has been partially in-filled with predominantly basaltic eruptive products with lithologies dominated by hyaloclastite, subaerial lava flows, and fine-grained tuffs, while edifices of icelandite, dacite, and rhyolite have also been emplaced (Stefansson, 1981; Saemundsson, 1991). Pleistocene hyaloclastites formed during subglacial eruptions, while Holocene (3 ka – present) subaerial lavas were emplaced during six major eruptions with an interval period of 250-1000 years (Seamundsson, 1991). This study focuses on Holocene (post-

This is the peer-reviewed, final accepted version for American Mineralogist, published by the Mineralogical Society of America.
The published version is subject to change. Cite as Authors (Year) Title. American Mineralogist, in press.
DOI: https://doi.org/10.2138/am-2022-8363. http://www.minsocam.org/

glacial) basalts and Pleistocene (subglacial) basaltic hyaloclastites currently undergoing intense surface hydrothermal alteration in the Námafjall area.

The Námafjall geothermal area lies at the southern edge of the Krafla volcano (Figure 1), where hydrothermal fluids reach the surface along faults. These hydrothermal fluids interact with basaltic hyaloclastites atop and along the margins of the Námaskarð hyaloclastite ridge, and with late Holocene basaltic lava flows at Hverir at its base. The Hverir geothermal field lies to the east of Námaskarð and is dominated by vigorous fumaroles along a fault, with abundant hot springs and mudpots on the downthrown side (Saemundsson et al., 2012). These hot springs and mudpots interact with surface materials derived from local drainages, including from the neighboring Námaskarð hill. Large circular fumarolic aprons (up to ~25 m diameter) that produce little to no volcanic vapors are scattered across the Late Holocene lava field nearby. One of these circular fumarolic aprons is the focus of the current study.

Methods

Site details

At the eastern edge of the Hverir hydrothermal area (Figure 1c), individual fumaroles emerge through Holocene lavas. This interaction leads to a concentric "bulls-eye" fumarolic apron, with higher temperatures and more significant sulfur precipitation and alteration at the center (Figure 2). At the largest of these fumaroles, we collected surface samples along a transect (targeting

obvious changes in color or appearance) in 2013 (samples I-V-13 5 through 14), and returned in 2014 to excavate shallow pits to collect samples at depth (Figure 2) and in 2016 for more detailed observations. From these shallow pits, we collected both altered soil and pieces of altered basaltic lava (abbreviated PAB, samples I-V-14 6 through 20). Temperature, distance from fumarole center, and depth (if appropriate) are reported for each sample.

All samples analyzed in this study are summarized in Table 1. Precipitate samples were collected by carefully scraping surface materials over a small area into a plastic sample bag, and altered soils were scooped using a spatula. Pieces of altered basalt (PABs) were collected along with enclosing soil from the pits. Temperatures were measured for each sample using a thermometer. A less altered "substrate" sample was collected from the same lava flow, away from the fumarole field.

Laboratory Analyses

Samples were air dried and ground using an agate mortar and pestle without the addition of liquids. The substrate (basalt) sample was powdered first using a Rocklabs Shatterbox, then powdered more finely by hand. Samples were mounted as random powders for X-ray Diffraction (XRD) and analyzed at UW Milwaukee (UWM) using a Bruker D8 Focus XRD (Cu tube, 0.02° 2θ step size, 2–60° 2θ, 1 s/step, scintillation detector: see McHenry et al., 2017). Phases were identified using Bruker's EVA software and the International Centre for Diffraction Data Powder Diffraction Files (ICDD PDF) 2 database for comparison. Presence, absence, and qualitative relative abundance (trace vs. major) were estimated by comparing peak heights.

208

209 Samples that were determined not to be dominated by sulfur-bearing phases based on XRD were
210 further prepared for X-ray Fluorescence (XRF) analysis. Powdered samples were dried overnight
211 at 105°C. A split of each dried sample was analyzed for loss on ignition (LOI) using a muffle
212 furnace. Another split (1.000 g) of the same dried powdered sample was then mixed with 10.000
213 g of a 50/50 Lithium Metaborate/ Lithium Tetraborate flux with an integrated LiBr non-wetting
214 agent and ~1 g of ammonium nitrate (oxidizer) in a platinum crucible and fused into a glass bead
215 using a Claisse M4 fluxer. Beads were then analyzed for major and minor elements using a
216 Bruker S4 Pioneer XRF, following methods of Byers et al. (2016). Concentrations were
217 calculated using a calibration curve based on eleven USGS rock standards. Since sulfur is
218 partially lost during the fusion process, select samples for which sufficient material was available
219 were also prepared as pressed pellets. 7.5 grams of dried, powdered sample was combined with
220 three GeoQuant wax binder pellets (0.94 g total) in a shatterbox, and then pressed at 25 tons for
221 one minute in an Atlas T25 semiautomatic press. Pellets were then analyzed by XRF with
222 concentrations determined using a calibration curve based on six USGS rock standards. Only
223 sulfur is reported from the pressed pellets, as the fused bead calibration is better for all other
224 elements. Methods, limits of detection, and analytical errors associated with both calibrations are
225 described in detail in Byers et al., 2016).

226

227 Seven thin sections and small chips of fresh and altered basalt pieces were analyzed by Scanning
228 Electron Microscopy (SEM). Thin sections and small chips of altered basalt were carbon coated
229 using an Edwards Coating System E306A and placed into a geologic thin section holder, and
230 small chips of altered basalt were mounted on an aluminum stub and embedded in epoxy to

expose a specific vesicle in-filling or exterior surface of interest. Samples were analyzed using a S-4800 Hitachi at UW Milwaukee, using a cold cathode field emitter in secondary electron or backscattered electron mode with an accelerating voltage of 15 kV, 10 uA emission current, and high probe current. Elemental compositions were determined qualitatively using an attached Energy-Dispersive X-Ray Spectrometer (EDS) and Bruker software.

Results

XRD results

XRD results (Table 1) reveal diverse mineral assemblages that vary depending on the specific environment. Sulfur-bearing minerals are abundant and include a wide range of sulfates (Ca (e.g. gypsum), Fe^{3+} (e.g. rhomboclase ($(H_5O_2)^+Fe^{3+}(SO_4)_2 \bullet 2(H_2O)$), ferricopiapite ($(Fe^{3+}_{2/3}Fe^{3+}_4(SO_4)_6(OH)_2 \bullet 20(H_2O)$), and mixed cation (e.g. natroalunite ($NaAl_3(SO_4)_2(OH)_6$), natrojarosite ($NaFe^{3+}(SO_4)_2(OH)_6$), jarosite ($KFe^{3+}(SO_4)_2(OH)_6$), and minamiite ($(Na,Ca,K)Al_3(SO_4)_2(OH)_6$) varieties), and elemental sulfur. Other phases include silica phases (amorphous silica, opal A, quartz, and cristobalite), oxides and hydroxides (anatase, hematite, goethite), clay minerals (smectite, kaolinite), and residual igneous phases (plagioclase, augite). As the clay size fraction was not separated for analysis, our characterization of the clay phases is limited to distinguishing between “smectite” (clays with first-order basal spacing around 14 angstroms, based on XRD) and kaolinite.

Figures 3 and 4 show representative XRD patterns that highlight the diversity in alteration mineralogy in the Hverir fumarole transect. Fumarolic alteration of the basaltic lava substrate and precipitation from fumarolic vapors, acting in conjunction with meteoric water, produced the following mineral assemblages: (i) elemental sulfur, at the fumarole vent and in lenses at greater distances, (ii) SiO_2-rich soils that include amorphous silica + anatase ± cristobalite ± quartz, sampled within ~2 meters of the vent, (iii) purple sediments that include natroalunite or jarosite ± hematite ± amorphous silica ± kaolinite, and (iv) red sediments that include hematite ± goethite ± jarosite. Other sulfates observed in samples collected near the Hverir fumarole include gypsum and minamiite (rarely observed, but both abundant in two samples each), and ferricopiapite and rhomboclase (only observed in one sample each). Along the margins of the acid-sulfate fumarole are clay-rich sediments that include smectite ± kaolinite ± anatase ± hematite and/or goethite.

XRF results

Altered rocks and soils in the vicinity of the fumaroles show a range of compositions (OM Tables 2-3), reflecting their formation environments and mineral assemblages. Heavily leached soils show elevated SiO_2 and TiO_2 concentrations (up to 93 wt% and 23 wt%, respectively), while red soils are elevated in Fe_2O_3 (up to 33 wt%). The less altered basaltic lava substrate had 49 wt% SiO_2 and relatively high iron (15.8 wt% Fe_2O_3T). TiO_2 for the substrate sample was 1.82 wt%, much lower than the TiO_2 observed in most of the altered samples. Sulfur was only analyzed for a subset of samples, but where analyzed shows enrichment in altered samples (0.2-5.4 wt% SO_4) compared to the substrate (0.11 wt% SO_4). Most cations (Na, K, Ca, Mg, Mn) are lower in the altered rocks and soils than in the substrate. These trends are shown in a spider plot,

276 in which the composition of altered basalt samples (PABs) are plotted against the less altered
277 substrate (Figure 5). Iron (reported at Fe_2O_3T) is variable throughout the study area, as reflected
278 by the colors observed during sampling.
279
280 Samples from the Hverir transect were subdivided into sediment, rock, and precipitate samples,
281 and pieces of altered basalt (designated PABs) that were collected along with surrounding
282 sediments. The composition of the PABs reflects the alteration of the basaltic lava in contact
283 with the fumarolic environment, and are plotted (in a spider plot) against the composition of the
284 basaltic lava in Figure 5. Differences in composition on a small spatial scale are evident for
285 individual samples that were subdivided (after collection) based on color and texture differences
286 observed within individual collected samples, in addition to expected differences between PABs
287 and their enclosing sediments. For example, samples IV-13-10 and IV-13-14 PAB were
288 separated into sub-samples IV-13-10W (much higher in SiO_2) and IV-13-10MIX (containing
289 elemental sulfur, and higher Fe_2O_3), and IV-13-14 PAB, where the pinker portion of the altered
290 rock (IV-13-14 PAB W+P) is higher in Fe_2O_3T, at 25.16 wt%, and contains abundant hematite,
291 compared to IV-13-14 PAB MIX, which has 9.00 wt% Fe_2O_3T, less than the substrate basalt. In
292 Figure 6, samples collected at the same distance from the fumarole are assigned the same symbol
293 (most come from different depths within the same pit, representing different colored layers or
294 lenses). The spread of compositions from samples from the same sampling locations
295 demonstrates small-scale variability that is largely independent of temperature and distance from
296 the fumarole.
297
298 **SEM/EDS results**

299

300 SEM/EDS analysis provided a detailed geochemical and mineralogical analysis for pieces of
301 altered basalt (PABs) from the Hverir fumarole transect for four distinct alteration groups: (i)
302 PABs in silica-rich soils (IV-13-7), (ii) PABs in purple sediments (IV-13-14 PAB), (iii) PABs in
303 red sediments (IV-13-13), and (iv) a slightly altered basalt along the distal margin (IV-13-11).
304 Examination of the interior of altered basalt shows varying degrees of alteration of primary
305 igneous textures and the precipitation of secondary minerals.

306

307 Pieces of altered basalt within silica-rich soils and colored sediments showed extensive alteration
308 and had few if any remaining primary phenocrysts, which were completely or partially replaced
309 by amorphous silica. In sample IV-13-7, a PAB from a red-orange soil, a small section of
310 primary minerals remained and exhibited extensively etched surfaces along augite and
311 plagioclase crystals (Figure 7a). Qualitative EDS results showed relict plagioclase laths with Al
312 and Si, while mobile elements Ca and Na were depleted. Titanomagnetite retained its skeletal
313 and cruciform texture, but with a notable depletion in Fe (referred to as 'ghost' texture by Urcia
314 et al., 2010). In one instance in this sample, FeOx spherules are observed near the cruciform
315 texture of titanomagnetites (Figure 7b).

316

317 Basaltic glass is completely absent in the silica-rich soils, whereas abundant sideromelane with
318 etched surfaces partially replaced by amorphous silica and possibly clays and iron oxides/
319 hydroxides is observed in the colored sediments (Sample IV-13-13, Figure 8a,b). In Figure 8b,
320 the dark layer near the rim of the sideromelane fragments likely represents palagonite, i.e. poorly
321 crystalline smectite-like material, based on its texture. In the less altered deposits at the margin

of activity (e.g. IV-13-11), basaltic glass is still preserved with minimal surface etching (Figure 8e). Secondary minerals observed by SEM for more altered samples were commonly associated with amorphous silica (Figure 9a,b for samples IV-13-13 and IV-13-14 PAB). The most frequently observed secondary minerals were members of the alunite-jarosite group and hematite. A microscopic needle-like barium and sulfur bearing mineral, presumably barite, was sparsely distributed in amorphous silica veins and surface coatings in the same sample (IV-13-13, Figure 8c). This sample also contains gypsum in amorphous silica veins (Figure 8d). XRD patterns for sample IV-13-13 did not show evidence for barite or gypsum, likely due to their minor abundance.

Discussion

Distribution of phases, based on environment

The Hverir fumarole transect revealed different mineral assemblages, following a coarse-scale concentric pattern from most altered (center) to least altered (margin), with local small-scale variation. The sample collected at the central fumarole vent consisted of almost pure elemental sulfur, surrounded by leached deposits dominated by amorphous silica with anatase (enriched in SiO_2 and TiO_2 and depleted in mobile elements). Elevated Fe_2O_3, associated with abundant hematite and goethite, is observed in some samples, primarily at greater distance from the vent (e.g. 33.46 wt% in IV-13-13, at 550 cm), though lenses of colored sediment with higher hematite and/or goethite are observed closer in (e.g. minor hematite in IV-13-7, at 120 cm). Figure 6 plots wt% Fe_2O_3T against other oxides, showing how it is depleted in SiO_2-rich samples and enriched

in P_2O_5-rich samples. Trends of wt% Fe_2O_3T vs. MgO, K_2O, and Al_2O_3 vary depending on the samples, but overall show increasing concentrations with increasing Fe_2O_3T. Clay minerals (including kaolinite and smectites) are rare in the vicinity of this fumarole, occurring in only the most distal pit (IV-14-17 and 18, at 800 cm), and are associated with elevated Al_2O_3. Sulfate minerals occur in about 1/3 of the samples from the fumarole transect, and include the Ca-sulfate mineral gypsum, members of the alunite-jarosite series (natroalunite, natrojarosite, and jarosite), Fe^{3+} sulfate minerals ferricopiapite and rhomboclase, and the mixed-cation, Al-rich sulfate mineral minamiite. Compared to the least altered sample of the basaltic substrate, all samples from the transect analyzed for sulfur have significantly elevated SO_4, even those for which sulfur-bearing phases (sulfur, sulfates) were not identified by XRD. This overall trend shows more reducing conditions at the fumarole vent (with elemental sulfur), while sulfates and oxides further from the vent reveal more oxidizing conditions. The amorphous silica and anatase rich zone surrounding the central vent reveals significant leaching and removal of most mobile elements. No systematic differences were observed between samples collected at depth and those collected near the surface, suggesting no significant change in redox conditions with shallow depth in the fumarole apron.

Element Mobility

The mobility of elements during alteration of basaltic lava by the Hverir fumarole can be traced by comparing the bulk compositions of pieces of altered basalt collected from shallow depths within the fumarole transect (the 2013 “PAB” samples) against the composition of unaltered basalt from the same lava flow (Fig 5). The sample farthest from the vent is the closest in

368 composition to the unaltered basalt, as expected. Sulfur is concentrated in all altered samples for
369 which sulfur was analyzed, added to the system by the fumarolic vapors. Also enriched in all but
370 the least altered sample are Si, Ti, and Zr, consistent with residual enrichment after acid-sulfate
371 leaching or mobile components. Al is depleted in all but the least altered sample, consistent with
372 its higher mobility in acidic systems. Except for the least altered samples near the margin, all
373 samples are depleted in most mobile elements, particularly Na, Ca, Mn, and Mg. K follows this
374 trend for some samples but retains its original concentration in samples that contain jarosite. Fe
375 varies from highly depleted to moderately enriched- a trend shown even more clearly in Fig 6. It
376 is most enriched in those samples that contain hematite as measured by XRD.
377
378 These trends show the strong influence of the acid-sulfate leaching environment. Extensive
379 leaching of mobile components (that are not included in the sulfur-bearing phases being
380 precipitated) leads to the residual enrichment of the least mobile elements- in this case Si, Ti, and
381 Zr. The Ti enrichment is exceptional- altered soil sample IV-13-8 has 23.16 wt% TiO_2 (though
382 the associated piece of altered basalt, IV-13-8PAB, has only 4.65 wt%), compared to 1.82 wt%
383 in the substrate basalt. Anatase is recognized in the XRD patterns of most samples, in some cases
384 (e.g. IV-13-6, 9, and 12) as the only crystalline phase in samples otherwise dominated by
385 amorphous silica.
386
387 **Alunite-Jarosite Group**
388
389 Members of the alunite-jarosite group are the most abundant sulfate phases observed in the
390 Hverir fumarole transect. They were identified in XRD patterns and by SEM (for samples IV-13-

3, IV-13-13, and IV-13-14 PAB), where they were observed to have distinct pseudo-cubic crystals, ranging from <5 to 20 μm in diameter (Figure 9). These minerals line interior walls of vesicles associated with amorphous silica and spheroidal FeOx. In other instances, dense aggregates partially fill vesicle interiors (e.g. IV-13-14 PAB).

The alunite-jarosite group minerals have an idealized chemical formula [$\mathbf{AB_3}(SO_4)_2(OH)_6$] where the A site is occupied by monovalent species K^+, Na^+, H_3O^+, while the B site is occupied by trivalent species Al^{+3} and Fe^{+3}. When Fe>Al the mineral is classified as jarosite, while those minerals with Al>Fe are in the alunite family. EDS provides reliable measurements for the alunite-jarosite compositions for the relative proportions of Fe and Al, but underestimates the amount of Na and K in the sample (see McCollom et al., 2013a). The qualitative chemical composition at Námafjall ranges from natroalunite to Al-bearing jarosite, and often shows enrichment of Fe and K in the crystal rims (Figure 10). Significant compositional zoning of the A site was also observed within individual crystals. Polished grain mounts showed similar pseudo-cubic morphology despite differences in chemical composition.

The alunite-jarosite group is known to range in composition as a result of significant solid solution mixing in the A site, while substitution of the B site is less common. Published data reports compositions that lie close to Fe and Al end-members, which likely reflects a miscibility gap between alunite and jarosite (Stoffregen et al., 2000; Papike et al., 2006). Possible explanations for the miscibility gap include differences in hydrolysis constants for dissolved Fe and Al species or oxidation state during deposition (Stoffregen et al., 2000; Papike et al., 2006, 2007). However, a few studies have reported intermediate compositions between natroalunite

414 and Al-bearing jarosite in zoned pseudocubic crystals that were found in the early stages of acid-
415 sulfate alteration of basalt in natural systems (Morris et al., 2005; McCollom et al., 2013a; Black
416 et al., in revision).
417
418 Compositional zonation of the A site in Hverir samples likely reflects local and temporal
419 variability in ambient fluid compositions during mineral precipitation (e.g. Juliani et al., 2005;
420 Papike et al., 2006). Although local basalts lack significant K-bearing minerals, the abundance of
421 jarosite can be attributed to the release of K from altered glass (e.g. IV-13-14 PAB). Na-jarosite
422 was associated with orange precipitates in fumarolic settings. The low water/rock ratio near the
423 fumarole (as opposed to hot springs) can allow Na and other soluble elements to be more readily
424 retained in the products of alteration.
425
426 The substitution of Fe and Al in the B site is likely attributed to local variation in the chemical
427 environment caused by the decomposition of Al-bearing (plagioclase) and Fe-bearing (olivine,
428 augite, primary oxide) minerals. This is supported by the wide compositional variation within an
429 individual sample. On the other hand, the enrichment of Fe in the crystal rims may reflect a
430 transition to more oxidizing conditions, which makes more ferric Fe available for precipitation in
431 the minerals (Papike et al., 2006). Regardless, EDS measurements record significant Fe-for-Al
432 substitution within the crystal structure in alunite-jarosite group minerals during acid-sulfate
433 alteration at Hverir, which corresponds well to alunite-jarosite observed in synthetic and natural
434 basaltic systems (Morris et al., 2005; McCollom et al., 2013a,b; Black et al., in revision).
435

Members of the alunite-jarosite group were often associated with spheroidal hematite. This observation suggests that the alunite-jarosite group may be unstable over time, eventually breaking down and forming more stable spheroidal hematite (Desborough et al., 2010; McCollom et al., 2013b).

Spheroidal Hematite

Abundant spheroidal Fe-oxides were observed in sulfate-rich fumarolic deposits (Figures 7, 9, and 11). In samples IV-13-13 and 14 PAB, two FeOx populations were observed with similar spheroidal shape: (i) micrometer-sized (typically ~1-3μm diameter) spherules observed forming dense clusters around basaltic glass fragments and relict plagioclase and (ii) larger (~5 to 20 μm diameter) individual spheroids that often form botryoidal clusters (Figure 11). FeOx spherules lining vesicles or exterior surfaces (see Figure 11a,b) are interpreted as hematite, which is abundant in the XRD patterns, though goethite is also identified in lesser abundances in sample IV-13-13. Additional spherules within the interior of the basalt were observed (e.g. Figure 11c). All examined FeOx spherules contain impurities of Al, Si, S, and P that may serve as a nucleation site for mineral formation (Golden et al., 2008). Spheroidal FeOx associated with the alunite-jarosite group and amorphous silica lining vesicle walls and exterior surfaces are a commonly found mineral assemblage in volcanic acid-sulfate environments (Morris et al., 2005; Bishop et al., 2007; McCollom et al., 2013a). Additionally, these FeOx spherules exhibit a radial growth pattern consisting of rods or fibers (see Figure 11d). Morphology, elemental composition, and association with Fe-bearing sulfates support the interpretation that spheroidal hematite in the fumarolic deposits is related to aqueous precipitation during acid-sulfate alteration of basalt.

459

460 The occurrence of spherules at Hverir provides direct evidence for the formation of spheroidal
461 hematite during acid-sulfate alteration, but it is unknown whether hematite formed from the
462 dissolution of basaltic precursors or through a multi-step process. The latter involves a simplified
463 two-step process: (i) the formation of Fe-bearing sulfates (e.g. jarosite) and (ii) the dissolution of
464 sulfates to form spheroidal hematite through forced hydrolysis. Morris et al. (2005) noted the
465 apparent absence of hematite in altered basaltic tephra at Mauna Kea where hydrothermal
466 solutions did not form sulfate minerals. This observation implied that the formation of jarosite
467 and Fe-bearing natroalunite under acid-sulfate conditions was a necessary precursor for the
468 formation of hematite spherules.

469

470 Published laboratory experiments support the multi-step hypothesis. Several studies have shown
471 that hematite spherules can directly precipitate from aqueous solutions during forced hydrolysis
472 at ~100°C (e.g. Kandori et al., 2000). Spheroidal growth is affected by a variety of factors that
473 include: anions (SO_4, Cl), super-saturation, extent of hydrolysis, viscosity of the medium, and
474 impurities (Golden et al., 2010). Golden et al. (2008) synthesized both jarosite and spheroidal
475 hematite from Mg-Al-Fe-SO_4-Cl solutions in the following reaction sequence: (i) initial
476 precipitation of metastable hydronium jarosite at pH 1.2-1.5, (ii) jarosite dissolution and
477 precipitation of an intermediate ferric hydroxyl species through forced hydrolysis that
478 polymerizes into hematite, and (iii) precipitation of hydronium alunite upon depletion of
479 hydronium jarosite. Hydrothermal acidic conditions and high Fe^{3+} concentrations promote the
480 formation of hematite over goethite (Cornell and Schwertmann, 2003). However, goethite is
481 predicted to form from the breakdown of jarosite under reducing conditions (King and

McSween, 2005), which is supported by observations in acid-mine drainage (AMD) environments (Fernández-Remolar et al., 2005). Elwood Madden et al. (2012) describe jarosite dissolution experiments under a range of different pH and temperature conditions, and found that iron (hydro)oxides formed quickly in experiments with pH >3.5. While various phases formed as initial reaction products (e.g. hematite, maghemite, schwertmannite, and ferrihydrite), reactions did lead to hematite over time. They observed goethite in only one reaction (at pH 4.4) and only as a minor phase, and postulate that goethite may not form as readily under water-limited Martian conditions. Both hematite and goethite were observed in the fumarole transect at Hverir, though hematite was more common and usually more abundant.

Phyllosilicates

Kaolin and smectite group minerals (as detectable using only bulk powder XRD) are the main phyllosilicates in the Hverir fumarole transect. Kaolinite is only observed in the most distal samples (IV-14-17 and 18, at 800 cm) and smectite is only identified in one sediment sample (IV-13-11, at 600 cm), alongside plagioclase and augite, reflecting a low degree of alteration. Increased distance from the pathway of hydrothermal fluids will raise the pH and neutralize the acidity within the system and, thereby, precipitate out minerals containing more mobile elements (e.g. Ca, Mg). The composition of smectite depends on a combination of several factors including the pH of the fluid, element mobility, and the pathway of the fluids. It is important to remember that the genesis of poorly crystalline smectite clays comes from the hydration of sideromelane fragments, i.e. palagonite. Through continued alteration, palagonite transforms into

smectite, hence, smectite can be an abundant mineral phase in areas of low surface activity further from the source of heat and fumarolic vapors.

Thermodynamic models indicate that most phyllosilicate formation is favored by moderate to alkaline pH conditions (e.g. Velde, 1995). However, kaolinite can precipitate at low pH (Fialips et al., 2000). The behavior of phyllosilicate stability in low pH systems with high ionic strength is not well understood. For example, Mg-smectites (e.g. saponite) are more susceptible to alteration in acid waters than Al-phyllosilicates. Even so, Story et al. (2010) showed that these phyllosilicates can persist in sediments saturated in acid-saline lakes in Western Australia. In addition, Peretyazhko et al. (2014) synthetically produced saponite and nontronite from the alteration of basaltic glass under mildly acidic conditions (pH 4). Also, Hynek et al. (2013) documented kaolinite in acid-sulfate alteration of basalts in fumaroles and hot springs with pH as low as 2 and montmorillonite at pH 4 at Cerro Negro volcano, Nicaragua. The presence of smectite at the outskirts of a fumarole apron, associated with both primary igneous phases and Fe-sulfate minerals, provides further evidence that smectite can form and persist under acid sulfate fumarolic conditions, in an area of low surface activity.

Silica and anatase

Most samples from the Hverir fumarole transect display a significant amorphous silica “hump” in their XRD patterns. Some samples (all from Pit 1, 200 cm from the Hverir fumarole: samples IV-14-6 and IV-14-8 through 12) contain cristobalite as well. Opal A was only observed in sample IV-14-6, in a white, fibrous coating of an altered basaltic fragment near the surface of the

same pit. Quartz was observed in two samples collected at or near the surface- one sandy sediment (sample IV-13-09) and one PAB (sample IV-13-14 PAB).

The abundant amorphous silica in the leached apron surrounding the fumarole, often associated with abundant anatase (and elevated concentrations of both SiO_2 and TiO_2 measured by XRF), is consistent with acid-sulfate leaching of the surrounding rocks and soils at low to moderate temperatures. Other elements are leached away, leaving a residual concentration of these less mobile elements. SiO_2 is initially housed in amorphous silica, while TiO_2 is housed within anatase.

Since the substrate is Holocene basaltic lava, quartz and cristobalite are not expected as primary volcanic minerals. Their presence within pieces of altered basalt rules out detrital contamination as a likely source (e.g., wind-blown from degrading rhyolites in the Krafla area), though this remains a possible source for the quartz observed in the sandy sediment sample (IV-13-09). While cristobalite is most often considered a high-temperature silica polymorph (if quenched rapidly from high temperatures, it can exist metastably at the surface), it can also form from the devitrification of volcanic glass (Heaney, 1994). Opal-CT, which consists of disordered mixtures of cristobalite and tridymite, can form authigenically within sediments (Heaney, 1994), though its XRD pattern reflects this disorder, with broader peaks than the sharp cristobalite peaks observed in this study (e.g. Graetsch, 1994). Cristobalite is also described in steam vent samples from Sulfur Banks at Kilauea, Hawaii, where Morris et al. (2000) attribute its formation to precipitation from dissolved SiO_2 under hydrothermal conditions. Quartz and cristobalite both generally require higher temperatures to form, above the range typically associated with surface

550 hydrothermal alteration, or longer periods of time, to reach a higher level of diagenetic
551 maturation. Estimates for the time it takes for opal-A formed through hydrothermal sinter
552 precipitation or acid-sulfate fumarole leaching to mature into quartz under terrestrial surface
553 conditions vary from thousands or tens of thousands of years (Herdianita et al., 2000; Rodgers et
554 al., 2002, 2004) to as little as hundreds of years (Taupo volcanic area: Lynne et al., 2007) or even
555 months (Lynne et al., 2006), depending on the specific conditions. These shorter episodes of
556 maturation are assisted by higher temperatures, such as those in persistent acid-sulfate fumarole
557 environments.
558
559 Anatase is a major mineral constituent on some of the acid leached samples, and in some cases is
560 the only crystalline phase (associated with amorphous silica). TiO_2 concentrations reach as high
561 as 23.16 wt% in one leached soil sample (IV-13-8), and a PAB collected at the same level (IV-
562 13-8-PAB) had 4.65 wt% TiO_2, significantly concentrated over the 1.82 wt% observed in the less
563 altered substrate. This overwhelming pattern of TiO_2 enrichment reveals significant acid leaching
564 and the removal of more mobile constituents, even silica, and demonstrates clearly that the
565 associated amorphous silica is associated with residual enrichment due to leaching, rather than
566 due to sinter precipitation (as might occur under more neutral conditions). With over 12x the
567 amount of TiO_2 in the leached sample with the highest concentration compared to the less altered
568 basalt, TiO_2 is clearly being enriched relative to SiO_2, and their residual enrichment thus does not
569 appear to be coupled. This contrasts with the observations of Morris et al. (2000) for Kilauea,
570 where TiO_2 is enriched at a more moderate level during fumarolic alteration of basalt, though
571 most Hverir samples from the current study show comparable levels of enrichment.
572

573 **Overall Fluid-Rock Interaction and Secondary Mineralogy at the Surface**

574

575 The alteration halos or aprons around fumaroles exhibit distinct mineralogical and geochemical
576 trends as the result of element mobility and the formation and precipitation of secondary
577 minerals. The dominant processes acting within a volcanic geothermal system include: (i) the
578 supply of acid and H_2S, (ii) the extent of the reaction and pH of the fluids, and (iii) the redox
579 conditions (Markússon and Stefánsson, 2011).

580

581 Acid-sulfate waters are produced upon the boiling of aquifer fluids, resulting in phase
582 segregation of the vapor/steam from the boiling water. Rising volcanic vapors enriched in H_2S
583 and CO_2 condense into oxygenated ground- and surface-waters where the H_2S is oxidized into
584 sulfuric acid and the CO_2 is mostly degassed (Kaasalainen & Stefánsson, 2012). The results are
585 acidic waters with pH <4 and reducing conditions that alter basalt in gas- (low water-rock ratios)
586 and fluid- (high water-rock ratios) dominated settings. The SEM analyses of altered basalts in the
587 current study show relict plagioclase and augite, largely replaced by an amorphous
588 aluminosilicate (Figure 7). Glass is not observed in highly altered samples, but can be seen
589 undergoing alteration in less altered samples (Figure 8).

590

591 In gas-dominated settings, such as the Hverir fumarole, secondary minerals can precipitate
592 directly from the volcanic vapors or during alteration of primary igneous phases. Sulfur-bearing
593 phases at the Hverir fumarole are limited to elemental sulfur at the source and sulfate minerals
594 further out, indicating more oxidizing conditions. No sulfide minerals were observed in the XRD
595 patterns for any samples from the Hverir fumarole, in contrast to what is observed in hot spring

596 and mud pot contexts to the west within the Hverir hydrothermal area (Mínguez et al., 2011) or
597 on the slopes or summit of neighboring Námaskarð hill (el-Maarry et al., 2017). The fumarole
598 environment thus appears to be significantly more oxidizing than the higher water/rock ratio hot
599 spring and mud pot environments of the same field.
600
601 **Fumarolic Alteration Model**
602
603 A conceptual model for fumarolic alteration illustrates what happens when volcanic vapors
604 interact with Holocene basalt (Figure 12). Fumarolic alteration of the high-Fe basaltic substrate
605 (sample IV-13-15) exhibited isochemical trends, where mobile cations were extremely depleted
606 near the discharge source (X_4 – Figure 13) but retained in the alteration apron (X_1 – Figure 13).
607 Here, the low-water rock environment effectively mobilized major rock-forming and trace
608 elements. Sulfur exhibits a slight enrichment in the silica-rich soils, but most is mobilized into
609 the purple and red sediments, likely through lateral transport. Dissolved metals were transported
610 in solution and precipitated as a variety of sulfate and oxide phases such as barite, gypsum,
611 alunite-jarosite group minerals, and hematite along exterior surfaces and vesicle walls. In the
612 purple and red sediments, Fe and Al mobility was lower because of a more oxidizing
613 environment, which enriched the samples in immobile ferric Fe. Both Fe and Al were
614 incorporated into Fe^{3+}-bearing sulfates and oxides (e.g. X_2, X_3 – Figure 13). These phases were
615 important secondary minerals in medium to low activity areas. The least altered basalts show
616 minimal leaching along the margins of surface activity, where only minor depletion of Mg, Ca,
617 and Na were observed.
618

The low levels of volcanic gas emissions at Hverir fumaroles may explain the lack of surface efflorescence (e.g. Fe^{2+}-sulfates), but sulfate precipitates were found in shallow depth profiles. Here, members of the alunite-jarosite group are the dominant sulfates. The dominance of Al-sulfates over other sulfate phases corresponds well to fumarolic gas emissions, where $Al^{3+} >> Ca^{2+} + Mg^{2+}$ (e.g. Hynek et al., 2013). Fe-bearing natroalunite, spheroidal hematite, and amorphous silica were commonly associated alteration minerals that formed along vesicle walls and exterior surfaces. These secondary phases have been observed in other basalt-hosted volcanic environments at Haleakala and Cerro Negro volcanoes (Bishop et al., 2007; McCollom et al., 2013b), and thus likely represent a key mineralogical assemblage of fumarolic acid-sulfate alteration.

Relevance to Martian Hydrothermal Systems

Extrapolation of the mineralogical and chemical trends associated with the Námafjall geothermal system to analogous environments on Mars requires the consideration of several factors. First, the basaltic composition in Iceland differs from that of Mars. Icelandic basalts have similar, albeit slightly lower, Fe, higher Al, and lower Mg than Martian basalts (Table 4). This is significant because substrate largely controls the aqueous geochemistry, which affects the secondary mineral phases present (e.g. Tosca et al., 2004). As a result, the basalt composition will control in part the relative abundance of secondary minerals. Second, Icelandic geothermal areas occur in open-system environments, where soluble salts and Mg, Ca, Na and other cations are leached out of the system by meteoric water. Today, Martian atmospheric conditions differ significantly from modern terrestrial conditions; however our understanding of atmospheric

conditions during the Hesperian-Noachian period is limited. The abundance of ferric minerals and phyllosilicates in Noachian terrains may indicate at least locally oxidizing conditions and/or abundant surface water that altered basaltic substrate. The gas chemistry is wholly unconstrained, but given the high levels of sulfur in Martian basalts, volcanism likely produced abundant volatiles in the form of SO_2 and/or H_2S gas (Gaillard et al., 2009).

Home Plate, Gusev crater. Gertrude Weise class soils were exposed by Spirit's right front wheel in the Eastern Valley between Home Plate and the Mitcheltree/Low Ridge complex. The light-toned soils are enriched in silica (as much as 91 wt% SiO_2), Ti, Cr, and Zn, while most other major elements show a downward trend in abundance with increasing element atomic number relative to typical Martian soils (Squyres et al., 2008). The hydrated silica phase is identified (using measurements of Spirit's mini-TES instrument, compared against laboratory spectra of different silica polymorphs and mixtures) as opal-A and no high-temperature silica phases (e.g. cristobalite or quartz) were observed, indicating a lack of diagenetic maturation (Ruff et al., 2011). The exact depositional mechanism, fluid-rock ratios, and environmental parameters for the silica-rich soils in the Eastern Valley are not well defined.

Eastern Valley soils and nodular outcrops are enriched in silica (~64-92 wt%) and titanium (0.42-1.74 wt%) and were initially interpreted as leached acid-sulfate fumarole deposits due to their proximity to the Paso Robles (e.g. Tyrone) class soils (Ming et al., 2006). The sulfate-rich soils and Fe^{3+}/Fe total indicate low pH and highly oxidizing conditions (Lane et al., 2008). Acid-sulfate alteration could explain the leaching of most minerals from Gusev basalts and the relative enrichment of the most insoluble components (e.g. SiO_2, TiO_2). However, the solubility of silica

665 is relatively independent of pH under acidic to neutral conditions (Alexander et al., 1954;
666 Krauskopf, 1956) and, therefore, the composition of the Si-rich deposits does not constrain the
667 pH of the fluids. Ruff et al. (2011) argued that the silica enrichment is the result of precipitation
668 of silica-enriched fluids in a hot spring setting rather than acid leaching. They favored near-
669 neutral hot spring sinter deposition, noting that the lack of sulfur enrichment was inconsistent
670 with acid-sulfate leaching. Furthermore, the high water-rock ratios associated with hot spring
671 settings would be necessary to transport excess sulfur out of the system. Ruff et al. (2019) have
672 also made a strong case for a hot spring (rather than pervasive fumarole) origin for the silica-rich
673 deposits based on morphological and stratigraphic evidence.
674
675 Námafjall has areas of enriched silica- (~75-92 wt%) and titanium- (~3-23 wt%) soils, as the
676 result of intense fumarolic acid-sulfate leaching. Samples of these deposits were dominated by
677 amorphous silica and anatase. As anatase was not observed in XRD patterns for the less altered
678 substrate, and since many of these silica-rich samples contain significantly higher TiO_2, this
679 anatase is interpreted as a secondary, residual phase that formed from the concentration of TiO_2
680 following leaching of other cations. Near-neutral sinter deposits were not observed at these sites
681 and all hydrothermal fluids measured during our field studies in Námafjall were acidic. Thus a
682 direct comparison between these two formation mechanisms cannot be assessed in this study,
683 though the high concentrations of TiO_2 observed are likely unique to acid-sulfate leaching, as
684 TiO_2 is not easily mobilized in aqueous solutions (e.g., Gray and Coolbaugh 1994) and thus not
685 enriched in amorphous silica deposits formed through precipitation.
686

687 Alternatively, low to moderate sulfur contents were observed in thick Si-rich soils (<1 m depth)
688 in the Hverir fumarolic apron, never exceeding ~1 wt% SO_4 in soil samples for which it was
689 analyzed, which is below all measured values for Eastern Valley materials on Mars, though
690 altered basalt pieces (PAB samples) from Hverir often had higher SO_4 (see OM Table 2). At
691 Hverir, amorphous silica and anatase were the dominant minerals near the vent (beyond the
692 elemental sulfur halo), though in one sampling pit at 200 cm distance from the vent, cristobalite
693 was also abundant, potentially indicating a higher degree of diagenetic maturity. Cristobalite was
694 not found in surface samples or in samples from any other pits at Hverir, suggesting a localized
695 occurrence. In sum, results show that silica deposits related to fumarolic alteration in the
696 Námafjall area exhibit highly variable sulfur enrichment, ranging from <2 to 65x greater than the
697 parent rock.
698
699 On Mars, Eastern Valley deposits did not exhibit other secondary minerals or other high-
700 temperature silica phases (such as cristobalite), as interpreted from mini-TES data. Ruff et al.
701 (2011) concluded that the lack of other mineral phases, especially sulfates, indicated a near-
702 neutral hot spring setting. However, our study (and Hynek et al., 2013) demonstrates that
703 fumarolic acid-leaching can remove most of the excess sulfur from the system and produce a
704 deposit dominated by amorphous silica (and anatase) with only minor sulfates, which are not
705 observed in most samples from the Hverir transect. These thick silica-rich soils generated by
706 acid-sulfate fumaroles may be an effective analog for Eastern Valley soils (e.g. Lefty Ganote and
707 Kenosha Comets). Therefore, the pH of the fluids and formation mechanism (near-neutral sinter
708 deposition versus acid-sulfate leaching) that formed the silica deposits in the Eastern Valley may
709 not be easily constrained by SO_3 concentrations and the presence or lack of associated sulfate

minerals, as this could be the result of either process. The morphologic and stratigraphic context cited by Ruff et al. (2019), and the lack of the extreme TiO_2 enrichments observed at Hverir in the Eastern Valley silica-rich deposits, are stronger justifications for a non-fumarole origin. However, Yen et al. (2008) acknowledge that Kenosha Comets has TiO_2 concentrations 50% higher than those observed in average basaltic soils and provisionally attribute their formation to a high-temperature acid bleaching process.

Jarosite and Spheroidal Hematite at Meridiani Planum. Jarosite ($KFe^{3+}_3(SO_4)_2(OH)_6$) is an important environmental indicator mineral, which has been detected by orbiters (e.g. Milliken et al., 2008; Farrand et al., 2009; Roach et al., 2010; Thollot et al., 2012; Bishop et al., 2021) and the Opportunity rover (e.g. Klingelhofer et al., 2004) in diverse geologic settings on Mars. In terrestrial environments, jarosite is typically found in low-pH volcanic sulfur-rich fumarolic deposits, acid-mine drainage, and saline-acid lakes (e.g. Elwood Madden et al., 2004; Tosca et al., 2005; Papike et al., 2006; Story et al., 2010). The stability of jarosite in terrestrial settings has placed constraints on the environmental conditions present in the sulfate-bearing rocks in the Burns Formation at Meridiani Planum that consists of ephemeral mildly to strongly acidic waters with a pH <4.5 and oxidizing conditions, since Fe must be present in ferric form (e.g. Burns, 1987; Tosca et al., 2005).

The presence of jarosite in the Meridiani outcrops would also place constraints on the conditions after deposition. Elwood-Madden et al. (2004) concluded that low water-rock ratios are needed to preserve the jarosite and Ca-sulfate weathering products, because progress towards equilibrium causes early-formed minerals to become unstable. Therefore, the presence of jarosite

733 in Meridiani outcrops indicates that basaltic weathering on Mars likely did not go to completion.
734 Limited water near the surface/subsurface would explain the presence of soluble sulfate-salts.
735 Perhaps, after deposition from an ephemeral hydrothermal or non-thermal aqueous solution, the
736 solution evaporated and stayed dry until the present day.
737
738 In terrestrial systems, jarosite is a relatively unstable mineral and breaks down to form Fe^{3+}
739 oxides and hydroxides; hematite and/or goethite, depending on the environmental conditions. At
740 Meridiani Planum, one proposed pathway to form hematite spherules involves the incongruent
741 dissolution of a jarosite precursor; both jarosite and hematite have been proposed to be products
742 of acid-sulfate alteration of basalt (Morris et al., 2005; Golden et al., 2008; Elwood Madden et
743 al., 2012; McCollom et al., 2013a). Námafjall FeOx spherules are closely associated with jarosite
744 and Fe-bearing natroalunite, providing a natural analog to further support this scenario.
745 McCollom et al.'s (2013a) work further confirms that hematite spherules can be formed from Fe-
746 bearing natroalunite in addition to jarosite by the same process.
747
748 Golden et al. (2008) presented the following model, which is also supported by our studies of
749 acid-sulfate alteration in basalt-hosted volcanic environments at Hverir, and studies elsewhere
750 (e.g. Morris et al., 2005; McCollom et al., 2013b). Acid-sulfate alteration of basaltic materials at
751 Meridiani Planum and Námafjall formed Fe- (e.g. jarosite or Fe-natroalunite), Ca- and Mg-
752 sulfates. The source of sulfur at Meridiani is uncertain and a recent review of the formation
753 models, considering mass balance, indicated that none of the proposed models can account for
754 the S enrichments (Hynek et al., 2019). The MER team infers that evaporative conditions of
755 acidic groundwater would enrich S concentrations to form sulfates (Grotzinger et al., 2005).

Alternatively, S enrichment could be associated with the condensation of fumarolic emissions and/or the exposure and oxidation of iron-sulfides in the presence of water (Knauth et al., 2005; McCollom & Hynek, 2005), processes both present at Námafjall. Acid-sulfate solutions would have quickly dissolved the primary igneous phases, a scenario supported by only residual presence of igneous Fe-bearing phases and plagioclase, and released Fe into solution to form jarosite and hematite (Glotch et al., 2006). Low water-rock ratios are inferred because the bulk chemical composition is basaltic when calculated as S-free (McCollom and Hynek, 2005; 2006; Morris et al., 2006; McCollom, 2018), indicating that mobile elements were not removed as would be expected at higher water-rock ratios.

More detailed studies are required to determine the characteristics of hematite at Hverir, but it seems likely that spheroidal hematite there may have similar properties to those synthesized by Golden et al. (2008), McCollom et al. (2013b), and Marcucci and Hynek (2014). Hverir spherules are also similar to spherules in other volcanic settings (e.g. Morris et al., 2005; McCollom et al., 2013a); though they are substantially smaller than those at Meridiani (which are ~40 to 400x larger than terrestrial hydrothermal spherules). This difference in size may be the result of high-temperature (>100°C) conditions, which would improve the kinetics of spheroidal hematite formation, whereas the Hverir spherules are found in samples at temperatures <70°C. Longer duration of aqueous activity is also inferred at Meridiani Planum, while the altered Hverir substrate was deposited ~6100 years ago and is therefore a geologically young feature. Additionally, the greater availability of Fe from Martian parent rocks compared to terrestrial basalts could also potentially influence the size and abundance of iron oxides. Prolonged acid-

778 sulfate alteration on Mars could help form more extensive hematite deposits and possibly alunite
779 within the altered siliciclastic materials.
780 Textural considerations, in additional to spherule size, limit the direct application of the Hverir
781 hematite spherules to those at Meridiani. The hematite spherules in the Hverir fumarole transect
782 was largely observed within vesicles or on interior surfaces within altered basaltic lava, which is
783 notably different from the siliciclastic environment in which the Meridiani hematite spherules are
784 found (e.g. McLennan et al., 2005). Hematite spherules from volcanic environments where
785 tephra (rather than lava) is the substrate, such as at Mauna Kea (Morris et al., 2005) would thus
786 be a better textural analog, though those spherules are also much smaller than the Meridiani
787 hematite. Morris et al. (2005) also note that not all of the hematite at Meridiani is in the form of
788 large spherules, and that spherules as small as the ones found in the Mauna Kea study (or the
789 current study) would not be imageable by the MI instrument on Opportunity. Temperature is
790 another consideration; if elevated temperatures are required to form gray hematite such as that at
791 Meridiani (e.g. Golden et al., 2008), hydrothermal processes may have been required (e.g.
792 McCollom and Hynek, 2005, 2006), though others have suggested mechanisms that could allow
793 for coarsely crystalline hematite to form at lower temperatures (e.g. Glotch et al., 2004, 2006;
794 Madden et al., 2010). The hematite at Hverir may have formed under either ambient or elevated
795 temperatures, as it is observed both in the hotter sediments closer to the fumarole and at the
796 margin.
797
798 The presence of jarosite at Meridiani was largely determined by Mössbauer spectra of outcrops.
799 A range of synthetic Fe-bearing natroalunite compositions produced by McCollom et al. (2013a)
800 yield spectra that closely resemble the Mössbauer spectral signature for jarosite, suggesting that

801 Fe^{3+}-bearing natroalunite should be considered as an alternative to a pure Fe^{3+}-sulfate component
802 in the Merdiani outcrop. The presence of Fe^{3+}-bearing natroalunite in the Burns Formation would
803 indicate variable Fe-Al substitution in the B site. Christensen et al. (2004) calculated that
804 samples for which jarosite was identified at Meridiani had insufficient Fe and too much sulfur
805 for all of the sulfate component to be jarosite. The APXS-measured Al_2O_3 concentrations of
806 "jarosite"-bearing samples at Meridiani are not consistently higher than those of other samples
807 (typically 6-8 wt. %: Rieder et al., 2004), though differences in the calculated abundances of
808 feldspars (the main host of Al in the assemblage) makes it difficult to assess the amount of Al
809 available for natroalunite.
810
811 If natroalunite, rather than jarosite, were the source of the "jarosite" signal in the Opportunity
812 Mössbauer data, then the environmental conditions during the formation of the Burns Formation
813 would be less well constrained. Fe-bearing natroalunites have stability ranges much higher than
814 jarosite, up to pH 7.5 and under less oxidizing conditions (e.g. Brown, 1971). Natroalunite is also
815 more stable than jarosite, which could affect the conditions required for its long-term
816 preservation on Mars (e.g. McCollom et al., 2013).
817
818 In terrestrial settings, intermediate compositions (between natroalunite and jarosite) reflect early
819 stages of acid-sulfate alteration of basaltic rocks in hydrothermal volcanic environments
820 (McCollom et al., 2013b). This observation may offer further support for the volcanic origin for
821 the inferred jarosite and hematite deposits at Meridiani (e.g. McCollom & Hynek, 2005). Fe-
822 bearing members of the alunite family would also considerably expand the range of possible
823 environmental conditions present at the time of formation. Alunite is thermodynamically stable

824 up to pH 7.5 and under less oxidizing conditions, and can precipitate from Fe^{2+} solutions (Burns,
825 1987). If further evidence determines the Martian 'blueberries' formed under hydrothermal
826 conditions, then this would suggest significantly different paleoenvironmental conditions at
827 Meridiani than models that propose low-temperature interaction of sediments with groundwater
828 (e.g. McLennnan et al., 2005).
829
830 **Implications**
831
832 The alteration mineral assemblages and patterns of element enrichment and depletion observed
833 in this Hverir fumarole are relevant to the interpretation of potentially hydrothermal deposits on
834 Mars, including silica-rich soils investigated by the Mars Exploration Rover (MER) Spirit in the
835 Columbia Hills and jarosite and hematite occurrences at Meridiani Planum, investigated by MER
836 Opportunity. Several key observations:
837
838 1) The co-occurrence of jarosite with smectitic clays show that these smectites formed under
839 acid-sulfate conditions in the vicinity of these fumaroles. Clay formation is often
840 attributed to neutral to alkaline fluids in models for early Mars (unlike sulfate-rich
841 deposits, attributed to later acidic conditions, e.g. Bibring et al., 2005). Clay formation
842 and/or stability under more acidic conditions is consistent with recent geochemical
843 modeling by Peretyazhko et al. (2018) and observations from Australian acid lakes (Story
844 et al., 2010) and other fumarolic environments (Hynek et al., 2013).
845

2) Amorphous silica rich deposits formed through acid-sulfate leaching in a fumarolic environment, yet many samples lack sulfate minerals. The lack of accessory sulfate minerals in hydrothermally-formed silica-rich deposits near Home Plate in the Columbia Hills has been interpreted to favor precipitation of silica sinters from near-neutral fluids, rather than acid-sulfate leaching (e.g. Ruff et al., 2011), though other lines of evidence, including morphology and stratigraphy, are now interpreted to favor a sinter model (e.g. Ruff et al., 2019).

3) The presence of cristobalite in fumarole-altered basalt confirms that this phase is not limited to volcanic or high-temperature hydrothermal environments and can precipitate in fumarolic environments under milder hydrothermal conditions through direct precipitation or the breakdown of basaltic glass.

4) The extreme concentration of TiO_2 (12x) in some fumarole-leached samples shows that TiO_2 enrichment can outpace SiO_2 enrichment in an acid-leaching environment and it may not be the most appropriate "immobile" element to use in determining the degree of leaching. While not enriched to the same level, the silica-rich soil Kenosha Comets from the Eastern Valley (Gusev crater, Mars) also has TiO_2 concentrations 50% higher than the likely precursor basalt (Yen et al., 2008).

5) These fumarole alteration deposits contain naturally occurring Fe-bearing natroalunite. Only limited solid solution between natroalunite and jarosite has been previously recognized (e.g. Papike et al., 2006). This is important because Fe-bearing natroalunite could have similar Mössbauer spectroscopy signatures to jarosite (e.g. McCollom et al.,

2013a,b), which could call into question the identification of jarosite at Meridiani Planum on Mars (e.g. Klingelhöfer et al., 2004). Natroalunite is less restricted in its pH range, and its presence (rather than jarosite) could allow a wider range of conditions that could have formed these sulfates on Mars.

6) Spheroidal hematite lining vesicle walls likely formed from the dissolution of Fe-bearing natroalunite and/or jarosite in Hverir fumaroles. This multistep process is similar to experiments conducted by Golden et al. (2008) and McCollom et al. (2013b), suggesting a pathway of formation for hematite spherules on Mars. If Fe-bearing natroalunite is the Fe^{3+}-sulfate component in the Burns Formation, this may be a key signature of hydrothermal acid-sulfate alteration, though the larger size and textural context of the Meridiani "blueberries" needs to be considered.

Together, these observations inform our interpretations of the environments under which fluid-rock interactions occurred on the surface of ancient Mars. Acid-sulfate fumarolic alteration (and associate leaching) is a plausible mechanism for the formation of some Martian deposits, including some silica-rich soils in the Columbia Hills (explored by the Spirit rover) and jarosite and hematite (explored by Opportunity). Smectitic clays can also form in these environments and co-exist with minerals typically associated with lower pH conditions (e.g. jarosite), and their presence thus does not preclude acid-sulfate hydrothermal processes.

Acknowledgments

The authors would like to thank Teri Gerard, Thomas McCollom, Ramy El-Maarry, and Sarah Black for their assistance in the field and Jordan Ludyan and Christopher Vickery for their help in the lab. This research was funded by grants from the UW-Milwaukee Research Growth Initiative (to McHenry) and NASA's Habitable Worlds (award NNX15AP15G to McHenry). Permission to export samples from Iceland was granted by the Icelandic Institute of Natural History.

Figures

Figure 1: Maps of (a) Iceland and the Krafla area, adapted from Gudmundsson and Arnorsson (2005), and (b and c) Námafjall geothermal field, with sampling sites from this study. Geologic map in (b) adapted from Saemundsson et al. (2012), satellite imagery in (c) from Google Earth.

Figure 2: Plan map and field photos for the sampled Hverir fumarole. (a) Map of surface sample locations and pits relative to the center of the fumarole apron. (b) field photograph of the fumarolic apron, with locations of shallow excavated pits. (c) close-ups of the shallow pits, with sample IDs.

Figure 3: Photos of the Hverir fumarole transect (including positions of four pits) and XRD patterns for samples from Pit 1 (200 cm from fumarole). The tan soil from the surface (IV-13-8R, 68.5°C) contains abundant amorphous silica and anatase, and minor quartz. IV-14-12, an orange soil sample collected at 18 cm depth (69.6°C), contains amorphous silica, cristobalite, goethite, and anatase. Sample IV-14-6, a white coating on a piece of altered basalt collected from 16 cm depth (73.2°C), contains amorphous silica, cristobalite, and anatase. Sample IV-14-9, purple sediment collected at 38 cm depth (71.3°C), contains amorphous silica, cristobalite, anatase, natroalunite, and hematite. Its elevated background in XRD is attributed to iron fluorescence, as this sample contains 15.40 wt% Fe_2O_3T, compared to 0.9-2.63 wt% of other samples reported from this pit.

Figure 4: Photos of the Hverir fumarole transect (including positions of surface samples) and XRD patterns for surface samples along it. Sample IV-13-5 was collected at the fumarole (97.8°C) and consists entirely of elemental sulfur. Sample IV-13-6 is surface sediment collected at 30 cm from the source (66.9°C), and consists entirely of amorphous silica and anatase, representing a leached deposit. Sample IV-13-14 PAB W+P consists of a while and pink altered rock collected at the surface 500 cm from the source, and contains amorphous silica, anatase, quartz, hematite, and minamiite. Sample IV-13-10 White consists of white sediment collected 550 cm from the source at 5 cm depth (17.2°C) and contains amorphous silica, anatase, gypsum, and rhomboclase. Sample IV-14-18 consists of red mud collected 800 cm from the source in a shallow pit (Pit 4) at 15 cm depth, and contains hematite, natroalunite, and kaolinite. Its high background in XRD is attributable to iron fluorescence, given the significant hematite occurrence in this sample.

Figure 5: Spider plot of altered basalt (PAB) samples from the Hverir fumarole transect normalized against the least altered basaltic substrate sample (IV-13-15). Missing data points indicate concentrations below the limits of detection. All samples indicate enrichment in sulfur compared to the fresh basalt, consistent with interactions with fumarolic sulfur, and all but the most distant from the center show elevated TiO_2, SiO_2, and Zr, consistent with residual enrichment through acid leaching. MnO, CaO, Na_2O, and K_2O are all significantly depleted in these leached samples. Sample IV-13-7-PAB is anomalous, as it is close to the fumarole center yet shows a less leached element abundance pattern similar to more distal samples.

Figure 6: Plots of XRF-derived bulk compositions for samples from the Hverir fumarole transect. All plots vs. Fe_2O_3T (wt%). The same symbol is used for all samples collected at a specific distance from the fumarole vent at the center of the feature. SiO_2 is highly concentrated (up to 92 wt%) in many samples, Fe_2O_3T is more enriched in lower SiO_2 samples. Al_2O_3, K_2O, and P_2O_5 abundances are typically higher for the higher Fe_2O_3T samples, while TiO_2 concentrations are highest in a few samples with low Fe_2O_3T. The variation exhibited by samples from the same distance show the degree of small-scale compositional heterogeneity.

Figure 7: SEM BSE images of a thin section of a heavily altered piece of basalt within red-orange soils (sample IV-13-7). (a) Small section of primary minerals in a highly leached basalt; Fe-S mineral is tentatively identified as pyrite. Altered clinopyroxene (augite) and plagioclase leached of mobile elements (e.g. Ca, Na) and replaced by amorphous alumino-silicate. (b) Altered titanomagnetite crystals (sample IV-13-7). Botryoidal growth of Fe-oxide spheroids forming in close association with titanomagnetite.

Figure 8: SEM image of altered basaltic glass fragments from sample IV-13-13 (a-d) and IV-13-11 (e). (a,b) Sideromelane fragments altered to Fe-hydr(oxides) and clays, in thin section. SEM BSE image of secondary minerals identified in amorphous silica veins. (c) SEM BSE image of needle-like barite crystals (labeled “ba”) and (d) SEM SE image of sample chip, showing authigenic gypsum (labeled “gy”) exhibits bladed star-shaped crystals on an amorphous silica spheroid from sample IV-13-13. (e) SEM BSE image of IV-13-11, showing less altered glass (gl) and basaltic lava fragments (bas) from the margin of activity (600 cm). sm = smectite.

Figure 9: Examples of the pseudocubic habit of the alunite-jarosite group from altered basalts from the Hverir geothermal field. Members of this group shown are natroalunite determined by EDS, except in (b), where jarosite was observed. (a) Interior vesicle wall with natroalunite, hematite, and amorphous silica (IV-13-14 PAB). (b) Adjacent vesicle walls with jarosite (light) forming on top of natroalunite (dark) with hematite and amorphous silica intermixed (IV-13-14 PAB). (c) Natroalunite cubes with dissolved interiors. (d) Natroalunite cubes with K-rich rims and Al-rich interiors (IV-13-14 PAB). (e) Psuedocubic natroalunite closely associated with small hematite spherules (IV-13-13). (f) Higher magnification image of (e), showing textural relationship between natroalunite and hematite (IV-13-3). NaL = natrojarosite, Si = amorphous silica, He = hematite, Jar = jarosite.

Figure 10: Natroalunite exhibits compositional zoning (IV-13-13). Alunite-jarosite group minerals have the chemical formula $[AB_3(SO_4)_2(OH)_6]$ (A site occupied by monovalent species K^+, Na^+, H_3O^+, while the B site is occupied by trivalent species Al^{+3} and Fe^{+3}). Zoned natroalunite (orange line = transect) shows Al-rich and Fe-depleted cores with elevated Fe and K along the rims. K is also slightly enriched in the core. Amorphous Silica (Si), Natroalunite (Nal).

Figure 11: Two distinct hematite spherule size populations: >3 and 5-20 micrometer range, with minor Al, Si, and S concentrations. (a) Hematite spheroids formed along the wall of vesicles and relict plagioclase crystals (IV-13-13). Inset shows an expanded view of spheroids. (b) Botryoidal morphology along vesicle walls with natroalunite cubes present (IV-13-14 PAB) and (c) Al-rich centers in Fe-oxide spherules may represent Al cores (Al) of remnant natroalunite (IV-13-13).

(d) Broken spherule shows fibrous/radial morphology of hematite. Hematite was confirmed by XRD analysis.

Figure 12: Conceptual model for the Hverir fumarolic apron. Alteration apron is up to 8 meters in diameter. The vertical shaded bar represents the oxidation front (between elemental sulfur and sulfate), as determined by surface mineralogy. The sulfur-rich layer found at depth may signify diffuse sulfur-bearing vapors that did not penetrate the surface. The maroon shaded area represents the changing color of the sediments, as amorphous silica dominated leached deposits give way to redder, more hematite-rich deposits. X1-X4 correspond to isocon plots in Figure 13.

Figure 13: Isocon plots for four samples from the Hverir fumarole, plotted relative to the less altered basaltic lava substrate (IV-13-15). Sample locations are marked as X1, X2, X3, and X4 on Figure 12. (X1) Along the distal margin (600 cm away, IV-13-11), a slightly altered basalt has minor depletions in Ca, Mg, Na, and Mn. (X2) In the red sediments (550 cm away, IV-13-13), Fe, K, and P are enriched and Al is slightly depleted, while, Ca, Mg, and Na are substantially depleted. (X3) Purple rocks and sediments (500 cm away, IV-13-14 PAB) exhibit pronounced depletions in most major elements, except for enrichments in Fe and K. (X4) Heavily altered basalts within the silica-rich soils (280 cm away, IV-13-12) are highly depleted of major cations with a residual enrichment of Si, Ti, and Zr. S is enriched in all samples.

Tables

1011 Table 1: Hverir fumarole transect sample descriptions, and XRD-based phase identifications for
1012 non-sulfates and sulfates.

1013

1014 Table 2 (Online Materials): XRF (major elements).

1015

1016 Table 3 (Online Materials): XRF (trace elements)

1017

1018 Table 4: Bulk chemistry, Iceland basalts vs. Mars

1019

1020 **References**

1021

1022 Abramov, O., and Kring, D.A. (2005). Impact-induced hydrothermal activity on early
1023 Mars. *Journal of Geophysical Research: Planets* 110(E12).

1024

1025 Alexander, G.B., Heston, W.M., and Iler, R.K. (1954) The solubility of amorphous silica in
1026 water, *Journal of Physical Chemistry* 58:453-455.

1027

1028 Bibring, J.-P. et al. (2005), Mars surface diversity as revealed by the OMEGA/Mars Express
1029 observations. Science 307: 1576–1581.

1030

1031 Bishop, J.L., Schiffman, P., Murad, E., Dyar, M.D., Drief, A., and Lane, M.D. (2007)
1032 Characterization of alteration products in tephra from Haleakala, Maui; a visible infrared
1033 spectroscopy, Mössbauer spectroscopy, XRD, EMPA and TEM study. *Clays and Clay Minerals*
1034 55:1-17.

1035

1036 Bishop, J.L., Noe Dobrea, E.Z., McKeown, N.K., Parente, M., Ehlmann, B.L., Michalski, J.R.,
1037 Milliken, R.E., Poulet, F., Swayze, G.A., Mustard, J.F., Murchie, S.L., Bibring, J.-P. (2008)
1038 Phyllosilicate diversity and past aqueous activity revealed at Mawrth Vallis, Mars. *Science*
1039 321:830-833.

1040

1041 Bishop, J.L., Weitz, C.M., Parente, M., Gross, C., Saranathan, A.M., Itoh, Y. and Al-Samir, M.,
1042 2021, March. Correlating Sulfates with the Aqueous Geochemical History at Juventae Chasma,
1043 Mars. In *Lunar and Planetary Science Conference* (No. 2548, p. 1082).
1044
1045 Björnsson, H. (1977). Konnun a joklum med rafsegulbylgjum. *Natturufraedingurinn* 47: 184-
1046 194.
1047
1048 Black, S.R., Hynek, B.M., McHenry, L.J., McCollom, T.M., Cameron, B.I., Glenister, C. (*in*
1049 *review*). Bulk mineralogy of surficial hydrothermal acid-sulfate deposits at Námafjall,
1050 Þeistareykir 1 Geothermal Field, and Hengill Volcano, Iceland: Implications for the
1051 identification and 2 interpretation of hydrothermal deposits on Mars. *Journal of Geophysical*
1052 *Research Planets.*
1053
1054 Bridges, J.C., and Schwenzer, S.P. (2012) The nakhlite hydrothermal brine on Mars. *Earth and*
1055 *Planetary Science Letters* 359:117-123.
1056
1057 Brown, J.B. (1971), Jarosite-goethite stabilities at 25 C, 1 ATM, Mineral. Deposita 6: 245-252.
1058
1059 Burns, R.G. (1987) Ferric sulfates on Mars. *Journal of Geophysical Research* 92:E570-E574.
1060
1061 Byers, H., McHenry, L.J., and Grundl, T.J. (2016) Forty-nine major and trace element
1062 concentrations measured in Soil Reference Materials NIST SRM 2586, 2587, 2709a, 2710a and

2711a using ICP-MS and Wavelength Dispersive-XRF. *Geostandards and Geoanalytical Research* 40:433-445.

Chojnacki, M., and Hynek, B.M. (2008) Geological context of water-altered minerals in Valles Marineris, Mars. *Journal of Geophysical Research* 113:E12005.

Christensen, P.R., Wyatt, M.B., Glotch, T.D., Rogers, A.D., Anwar, S., Arvidson, R.E., Bandfield, J.L., Blaney, D.L., Budney, C., Calvin, W.M. and Fallacaro, A., 2004. Mineralogy at Meridiani Planum from the Mini-TES experiment on the Opportunity Rover. *Science* 306: 1733-1739.

Cornell, R.M., and Schwertmann, U., (2003) The Iron Oxides: Structure, Properties, Reactions, Occurrences and Uses. Wiley-VCH, Weinheim.

Desborough, G.A., Smith, K.S., Lowers, H.A., Swayze, G.A., and Hammarstrom, J.M. (2010) Mineralogical and chemical characteristics of some natural jarosites. *Geochimica et Cosmochimica Acta* 74:1041-1056.

Ehlmann, B.L., Mustard, J.F., Swayze, G.A., Clark, R.N., Bishop, J.L., Poulet, F., Marais, D.J.D., Roach, L.H., Milliken, R.E., Wray, J.J., Barnouin-Jha, O., Murchie, S.L. (2009) Identification of hydrated silicate minerals on Mars using MRO-CRISM: Geologic context near Nili Fossae and implications for aqueous alteration. *Journal of Geophysical Research* 114:E00D08.

Ehlmann, B.L., Mustard, J.F., Clark, R.N., Swayze, G.A., and Murchie, S.L. (2011). Evidence for low-grade metamorphism, hydrothermal alteration, and diagenesis on Mars from phyllosilicate mineral assemblages. *Clays and Clay Minerals* 59(4):359-377.

Ehlmann, B.L., and Mustard, J.F. (2012) An in-situ record of major environmental transitions on early Mars at Northeast Syrtis Major. *Geophysical Research Letters* 39:L11202.

Ehlmann, B.L., and Edwards, C.S. (2014). Mineralogy of the Martian surface. *Annual Review of Earth and Planetary Sciences* 42:291-315.

El-Maarry M. R., Black S. R., Hynek B. M. and McHenry L. J. (2017) Mineralogy of Fumarolic Deposits from Iceland as Analogs for Ancient Hydrothermal Systems on Mars: Role of Temperature. In *Lunar and Planetary Science Conference*: 2870–2871.

Elwood Madden, M.E., Bodner, R.J., and Rimstidt, J.D. (2004) Jarosite as an indicator of water-limited chemical weathering on Mars. *Nature* 431:821-823.

Elwood Madden, M.E., Madden, A.S., Rimstidt, J.D., Zahrai, S.K., Kendall, M.R., and Miller, M.A. (2012) Jarosite dissolution rates and nanoscale mineralogy. *Geochimica et Cosmochimica Acta* 91:306-321.

1108 Farrand, W.H., Glotch, T.D., Rice Jr, J.W., Hurowitz, J.A. and Swayze, G.A., 2009. Discovery
1109 of jarosite within the Mawrth Vallis region of Mars: Implications for the geologic history of the
1110 region. *Icarus*, *204*(2), pp.478-488.
1111
1112 Fernández-Remolar, D., Morris, R.V., Gruener, J.E., Amils, R., and Knoll, A.H. (2005) The
1113 Rio Tinto Basin, Spain: Mineralogy, sedimentary geobiology, and implications for
1114 interpretation of outcrop rocks at Meridiani Planum, Mars. *Earth and Planetary*
1115 *Science Letters* 240:149-167.
1116
1117 Fialips, C-I., Petit, S., Decarreau, A., and Beaufort, D. (2000) Influence of synthesis pH on
1118 kaolinite "crystallinity" and surface properties. *Clays and Clay Minerals* 48:173-184.
1119
1120 Fraeman, A.A., Ehlmann, B.L., Arvidson, R.E>, Edwards, C.S., Grotzinger, J.P., Milliken, R.E.,
1121 Quinn, D.P., Rice, M.S. (2016) The stratigraphy and evolution of lower Mount Sharp from
1122 spectral, morphological, and thermophysical orbital data sets, *Journal of Geophysical Research*
1123 *Planets* 121:1713-1736.
1124
1125 Gaillard, F., and Scaillet, B. (2009) The sulfur content of volcanic gases on Mars. *Earth and*
1126 *Planetary Science Letters* 279:34-43.
1127
1128 Geptner, A.R., Ivanovskaya, T.A., and Pokrovskaya, E.V. (2005) Hydrothermal fossilization of
1129 microorganisms at the Earth's surface in Iceland. *Lithology and Mineral Resources* 40: 505-520.
1130

1131 Geptner, A.R., Ivanovskaya, T.A., Pokrovskaya, E.V., Lyapunov, S.M., Savichev, A.T.,
1132 Gorbunov, A.V., and Gor'kova, N.V. (2007) Hydrothermally altered hyaloclastites at the earth's
1133 surface in the rift zone of iceland; problem of the biochemogenic accumulation of trace elements.
1134 *Lithology and Mineral Resources* 42:453-476.
1135
1136 Glotch, T.D., Morris, R.V., Christensen, P.R. and Sharp, T.G., 2004. Effect of precursor
1137 mineralogy on the thermal infrared emission spectra of hematite: Application to Martian
1138 hematite mineralization. *Journal of Geophysical Research: Planets*, *109*(E7).
1139
1140 Glotch, T.D., Christensen, P.R. and Sharp, T.G., 2006. Fresnel modeling of hematite crystal
1141 surfaces and application to martian hematite spherules. *Icarus*, *181*(2), pp.408-418.
1142
1143 Golden, D.C., Ming, D.W., Morris, R.V., and Graff, T.G. (2008) Hydrothermal synthesis of
1144 hematite spherules and jarosite: Implications for diagenesis and hematite spherule formation in
1145 sulfate outcrops at Meridiani Planum, Mars. *American Mineralogist* 93:1201-1214.
1146
1147 Golden, D.C., Ming, D.W., and Morris, R.V. (2010) Spherulitic growth of hematite under
1148 hydrothermal conditions; insights into the growth mechanism of hematite spherules at Meridiani
1149 Planum, Mars. *Abstracts of Papers Submitted to the Lunar and Planetary Science Conference*
1150 41, Abstract 2541.
1151
1152 Graetsch, H. (1994). Structural characteristics of opaline and microcrystalline silica minerals. In:
1153 Hearney, P.J., Prewitt, C.T., Ginnes, G.V., Eds. Silica: Physical behavior, geochemistry, and

materials applications. Reviews in Mineralogy V. 29. Mineralogical Society of America, Washington, D.C., 209-232.

Gray, J.E., and Coolbaugh, M.F. (1994). Geology and geochemistry of Summitville, Colorado; an epithermal acid sulfate deposit in a volcanic dome. *Economic Geology* 89: 1906-1923.

Grotzinger, J. P., Arvidson, R.E., Bell, J.F.III, Calvin, W., Clark, B.C., Fike, D.A., Golombek, M., Greeley, R., Haldemann, A., Herkenhoff, K.E., Jolliff, B.L., Knoll, A.H., Malin, M., McLennan, S.M., Parker, T., Soderblom, L., Sohl-Dickstein, J.N., Squyres, S.W., Sullivan, R., Tosca, N.J., and Watters, W.A. (2005) Stratigraphy and sedimentology of a dry to wet eolian depositional system, Burns formation, Meridiani Planum, Mars. *Earth and Planetary Science Letters* 240:11-72.

Gudmundsson, B.T., and Arnórsson, S. (2002) Geochemical monitoring of the Krafla and Námafjall geothermal areas, N-Iceland. *Geothermics* 31:195-243.

Gudmundsson, B.T., and Arnórsson, S. (2005) Secondary mineral-fluid equilibria in the Krafla and Námafjall geothermal systems, Iceland. *Applied Geochemistry* 20:1607-1625.

Hausrath, E.M., Golden, D.C., Morris, R.V., Agresti, D.G., and Ming, D.W. (2013) Acid sulfate alteration of fluorapatite, basaltic glass and olivine by hydrothermal vapors and fluids: Implications for fumarolic activity and secondary phosphate phases in sulfate-rich Paso Robles soil at Gusev Crater, Mars. *Journal of Geophysical Research* 118:1-13.

Heaney, P.J. (1994). Structure and chemistry of the low-pressure silica polymorphs. In: Heaney, P.J., Prewitt, C.T., Ginnes, G.V., Eds. Silica: Physical behavior, geochemistry, and materials applications. Reviews in Mineralogy V. 29. Mineralogical Society of America, Washington, D.C., 1-40.

Herdianita, N.R., Browne, P.R.L., Rodgers, K.A., and Campbell, K.A. (2000) Mineralogical and textural changes accompanying ageing of silica sinter. *Mineralium Deposita* 35:48-62.

Hynek, B.M., McCollom, T.M., Marcucci, E.C., Brugman, K., and Rogers, K.L. (2013). Assessment of environmental controls on acid-sulfate alteration at active volcanoes in Nicaragua: Applications to relic hydrothermal systems on Mars. *Journal of Geophysical Research: Planets* 118:2083-2104.

Hynek, B.M., Rogers, K.L., Antunovich, M., Avard, G., Alvarado, G.E. (2018). Lack of microbial diversity in extreme Mars analog settings: Poás volcano, Costa Rica, *Astrobiology* 18, DOI: 10.1089/ast.2017.1719.

Juliani, C., Rye, R.O., Nunes, C.M.D., Snee, L.W., Correa, R.H., Monteiro, L.V.S., Bettencourt, J.S., Neumann, R., and Neto, A.A. (2005) Paleoproterozoic high-sulfidation mineralization in the Tapajos gold province, Amazonian Craton, Brazil: Geology, mineralogy, alunite argon age, and stable-isotope constraints. *Chemical Geology* 215:95-125.

1200 Kaasalainen, H., and Stefánsson, A. (2011) Sulfur speciation in natural hydrothermal waters,
1201 Iceland. *Geochimica et Cosmochimica Acta* 75:2777-2791.
1202
1203 Kaasalainen, H., and Stefánsson, A. (2012) The chemistry of trace elements in surface
1204 geothermal waters and steam, Iceland. *Chemical Geology* 330-331:60-85.
1205
1206 Kandori, K., Sakai, J., Ishikawa, T. (2000) Definitive effects of chloride ions on the formation of
1207 spherical hematite particles in a forced hydrolysis reaction. *Physical Chemistry Chemical*
1208 *Physics* 2:3293-3299.
1209
1210 King, P.L. and McSween, H.Y.Jr. (2005) Effects of H (sub 2) O, pH, and oxidation state on
1211 the stability of Fe minerals on Mars. *Journal of Geophysical Research* 110:E12S10.
1212
1213 Klingelhöfer, G., Morris, R.V., Bernhardt, B., Schröder, C., Rodionov, D.S., de Souza, P. A. Jr.,
1214 Yen, A., Gellert, R., Evlanov, E.N., Zubkov, B., Foh, J., Bonnes, U., Kankeleit, E., Gu¨lich, P.,
1215 Ming, D.W., Renz, F., Wdowiak, T., Squyres, S.W., and Arvidson, R.E. (2004) Jarosite and
1216 Hematite at Meridiani Planum from Opportunity's Mössbauer Spectrometer. *Science* 206:1740-
1217 1745.
1218
1219 Knauth, L.P., Burt, D.M., and Wohletz, K.H. (2005) Impact origin of sediments at the
1220 Opportunity landing site on Mars. *Nature* 438:1123-1128.
1221

1222 Krauskopf, K.B. (1956), Dissolution and precipitation of silica at low temperatures. *Geochimica*
1223 *et Cosmochimica Acta* 10:1-26.
1224
1225 Lane, M.D., Bishop, J.L., Dyar, M.D., King, P.L., Parente, M., and Hyde, B.C. (2008)
1226 Mineralogy of the Paso Robles soils on Mars. *American Mineralogist* 93:728-739.
1227
1228 Langevin, Y., Poulet, F., Bibring, J., Gondet, B., and Hanson, B. (2005) Sulfates in the north
1229 polar region of Mars detected by OMEGA/Mars Express. *Science* 307:1584-1586.
1230
1231 Lynne, B.Y., Campbell, K.A., Perry, R.S., Browne, P.R.L., and Moore, J.N. (2006) Acceleration
1232 of sinter diagenesis in an active fumarole, Taupo volcanic zone, New Zealand. *Geology* 34:749-
1233 752.
1234
1235 Lynne, B.Y., Campbell, K.A., James, B.J., Browne, P.R.L., and Moore, J. (2007) Tracking
1236 crystallinity in siliceous hot-spring deposits. *American Journal of Science* 307:612-641.
1237
1238 Madden, A.S., Hamilton, V.E., Madden, M.E., Larson, P.R. and Miller, M.A., 2010. Low-
1239 temperature mechanism for formation of coarse crystalline hematite through nanoparticle
1240 aggregation. *Earth and Planetary Science Letters*, *298*(3-4), pp.377-384.
1241
1242 Mangold, N., Carter, J., Poulet, F., Dehouck, E., Ansan, V., and Loizeau, D. (2012) Late
1243 Hesperian aqueous alteration at Majuro crater, Mars. *Planetary and Space Science* 72:18-30.
1244

Marcucci, E. C., B. M. Hynek, K. S. Kierein-Young, and K. L. Rogers, Visible to near-infrared spectroscopy of volcanic acid-sulfate weathering systems in Nicaragua: Analogs for early Mars alteration, *Journal of Geophysical Research - Planets*, 118, 2213–2233, doi:10.1002/jgre.20159, 2013.

Marcucci, E.C., Hynek, B.M. (2014). Laboratory simulations of acid-sulfate weathering under volcanic hydrothermal conditions: Implications for early Mars. *Journal of Geophysical Research Planets* 119:679-703.

Markússon, S.H., and Stefánsson, A. (2011) Geothermal surface alteration of basalts, Krýsuv k Iceland; alteration mineralogy, water chemistry and the effects of acid supply on the alteration process. *Journal of Volcanology and Geothermal Research* 206:46-59.

McCollom, T.M., Hynek, B.M., Rogers, K., Moskowitz, B., Berquó, T.S. (2013a) Chemical and mineralogical trends during acid-sulfate alteration of pyroclastic basalt at Cerro Negro volcano and implications for early Mars. *Journal of Geophysical Research: Planets* 118:1719-1751.

McCollom, T.M., Robbins, M., Moskowitz, B., Berquo, T.S., Joens, N., and Hynek, B.M. (2013b) Experimental study of acid-sulfate alteration of basalt and implications for sulfate deposits on Mars. *Journal of Geophysical Research: Planets* 118:577-614.

McCollom, T.M., and Hynek, B.M. (2005) A volcanic environment for bedrock diagenesis at

1268 Meridiani Planum on Mars. *Nature* 438:1129-1131.

1269

1270 McCollom, T.M., Hynek, B.M. (2006). Bedrock formation at Meridiani Planum: Reply. Nature
1271 443: E2.

1272

1273 McCollom, T. M., & Hynek, B. (2021). Geochemical data indicate highly similar sediment
1274 compositions for the Grasberg and Burns formations on Meridiani Planum, Mars. *Earth and*
1275 *Planetary Science Letters*, *557*, 116729.

1276

1277 McHenry, L.J., Carson, G.L., Dixon, D. T., Vickery, C.L. (2017). Secondary minerals associated
1278 with Lassen fumaroles and hot springs: Implications for martian hydrothermal deposits.
1279 American Mineralogist 102: 1418-1434. DOI: 10.2138/am-2017-5839

1280

1281 McHenry, L.J., Chevrier, V., Schröder, C., 2011. Jarosite in a Pleistocene East African saline-
1282 alkaline paleolacustrine deposit: Implications for Mars aqueous geochemistry. Journal of
1283 Geophysical Research 116: E04002. doi:10.1029/2010JE003680

1284

1285 McLennan, S., Bell, J.F., Calvin, W.M., Christensen, P.R., Clark, B.C., De Souza, P.A., Farmer,
1286 J.D., Farrand, W., Fike, D.A., Gellert, R., Ghosh, A., Glotch, T.D., Grotzinger, G., Knoll, A.H.,
1287 Learner, Z., Malin, M., McSween, H.Y., Pocock, J., Ruff S.W., Soderblom, L., Squyres, S.W.,
1288 Tosca, N.J., Watters, W.A., Wyatt, M.B., and Yen, A. (2005). Provenance and diagenesis of the
1289 evaporate-bearing Burns Formation, Meridiani Planum, Mars. *Earth and Planetary Science*
1290 *Letters* 240:95-121.

McSween, H.Y.J., Taylor, G.J., and Wyatt, M.B. (2009) Elemental composition of the Martian crust. *Science* 324:736-739.

Milliken, R.E., Grotzinger, J.P., and Thomson, B.J. (2010) Paleoclimate of Mars as captured by the stratigraphic record in Gale Crater. *Geophysical Research Letters* 37:L04201.

Milliken, R.E. et al. (2008) Opaline silica in young deposits on Mars. *Geology* 36:847-850.

Ming, D.W., Mittlefehldt, D.W., Morris, R.V., Golden, D.C., Gellert, R., Yen, A., Clark, B.C., Squyres, S.W., Farrand, W.H., Ruff, S.W., Arvidson, R.E., Klingelhöfer, G., McSween, H.Y., Rodionov, D.S., Schröder, X., de Souza, P.A.Jr., and Want, A. (2006) Geochemical and mineralogical indicators for aqueous processes in the Columbia Hills of Gusev crater, mars. *Journal of Geophysical Research* 111:E02S12.

Mínguez, H.A., Ortega, L., Lunar, R., Martínez-Frías, J., and Piña, R. (2011) Mineralogy of the Hydrothermal Alteration in the Námafjall Geothermal Field (Iceland). *MACLA. Revista Española de la Sociedad de Mineralogia* 15:25-26.

Morris, R.V., Rampe, E.B., Vaniman, D.T., Christoffersen, R., Yen, A.S., Morrison, S.M., et al. (2020). Hydrothermal precipitation of sanidine (adularia) having full Al,Si structural disorder and specular hematite at Maunakea volcano (Hawai'i) and at Gale Crater (Mars). Journal of Geophysical Research: Planets, 125, e2019JE006324. https://doi.org/10.1029/2019JE006324

Morris, R.V., Vaniman, D.T., Blake, D.F., Gellert, R., Chipera, S.J., Rampe, E.B., ... & Yen, A. S. (2016). Silicic volcanism on Mars evidenced by tridymite in high-SiO2 sedimentary rock at Gale crater. *Proceedings of the National Academy of Sciences*, 113:7071-7076.

Morris, R.V., Klingelhöfer, G., Schröder, C., Fleischer, I., Ming, D.W., Yen, A.S., Gellert, R., Arvidson, R.E., Rodionov, D.S., Crumpler, L.S., Clark, B.C., Cohen, B.A., McCoy, T.J., Mittlefehldt, D.W., Schmidt, M.E., de Souza, P.A.Jr., and Squyres, S.W. (2008) Iron mineralogy and aqueous alteration from Husband Hill through Home Plate at Gusev crater, Mars: Results from the Mössbauer instrument on the Spirit Mars Exploration Rover. *Journal of Geophysical Research* 113:E12S42.

Morris, R.V., Ming, D.W., Graff, T.G., Arvidson, R.E., Bell, J.F. III, Squyres, S.W., Mertzman, S.A., Gruener, J.E., Golden, D.C., Le, L., and Robinson, G.A. (2005) Hematite spherules in basaltic tephra altered under aqueous, acid-sulfate conditions on Mauna Kea volcano, Hawaii; possible clues for the occurrence of hematite-rich spherules in the Burns Formation at Meridiani Planum, Mars. *Earth and Planetary Science Letters* 240:168-178.

Morris, R.V., Golden, D.C., Bell III, J.F., Shelfer, T.D., Scheinost, A.C., Hinman, N.W., Furniss, G., Mertzman, S.A., Bishop, J.L., Ming, D.W. and Allen, C.C., 2000. Mineralogy, composition, and alteration of Mars Pathfinder rocks and soils: Evidence from multispectral, elemental, and magnetic data on terrestrial analogue, SNC meteorite, and Pathfinder samples. *Journal of Geophysical Research: Planets*, *105*(E1): 1757-1817.

Nachon, M., Clegg, S.M., Mangold, N., Schröder, S., Kah, L.C., Dromart, G., Ollila, A., Johnson, J.R., Oehler, D.Z., Bridges, J.C., Le Mouélic, S., Forni, O., Wiens, R.C., Anderson, R.B., Blaney, D.L., Bell, J.F.III, Clark, B., Cousin, A., Dyar M.D., Ehlmann B., Fabre C., Gasnault, O., Grotzinger, J., Lasue, J., Lewin, E., Léveillé, R., McLennan, S., Maurice, S., Meslin, P.-Y., Rapin, W., Rice, M., Squyres, S.W., Stack, K., Sumner, D.Y., Vaniman, D., and Wellington, D. (2014) Calcium sulfate veins characterized by ChemCam/Curiosity at Gale crater, Mars. Journal of Geophysical Research: 119, 1991–2016.

Nordstrom, D.K., and Alpers, C.N. (1999) Geochemistry of acid mine waters. *Reviews in Economic Geology* 6A:133-160.

Osinski, G.R., Tornabene, L.L., Banerjee, N.R., Cockell, C.S., Flemming, R., Izawa, M.R.M., McCutcheon, J., Parnell, J., Preston, L.J., Pickersgill, A.E., Pontefract, A., Sapers, H.M., Southam, G. (2013). Impact-generated hydrothermal systems on Earth and Mars. *Icarus*, 224(2), 347-363.

Papike, J.J., Karner, J.M., and Shearer, C.K. (2006) Comparative planetary mineralogy; implications of martian and terrestrial jarosite; a crystal chemical perspective. *Geochimica et Cosmochimica Acta* 70:1309-1321.

1358 Peretyazhko, T., Sutter, B., and Ming, D.W. (2014) Alteration of basaltic glass to Mg/Fe
1359 smectite under acidic conditions: A potential smectite formation mechanisms on Mars. 51st Clay
1360 Minerals Society Meeting; 17-21 May 2014; College Station, TX; United States.
1361
1362 Peretyazhko, T.S., Niles, P.B., Sutter, B., Morris, R.V., Agresti, D.G., Le, L., and Ming, D.W.
1363 (2018). Smectite formation in the presence of sulfuric acid: Implications for acidic smectite
1364 formation on early Mars. *Geochimica et Cosmochimica Acta* 220: 248-260.
1365
1366 Rampe, E.B., Bristow, T.F., Morris, R.V., Morrison, S.M., Achilles, C.N., Ming, D.W., et al.
1367 (2020). Mineralogy of Vera Rubin ridge from the Mars Science Laboratory CheMin instrument.
1368 *Journal of Geophysical Research: Planets* 12: e2019JE006306.
1369
1370 Reardon, E.J., and Beckie, R.D. (1987) Modelling chemical-equilibria of acid-mine drainage -
1371 the FeSO4-H2SO4-H2O system. *Geochimica et Cosmochimica Acta* 51:2355-2368.
1372
1373 Rieder, R., Gellert, R., Anderson, R.C., Brückner, J., Clark, B.C., Dreibus, G., Economou, T.,
1374 Klingelhöfer, G., Lugmair, G.W., Ming, D.W. and Squyres, S.W., 2004. Chemistry of rocks and
1375 soils at Meridiani Planum from the Alpha Particle X-ray Spectrometer. *Science* 306: 1746-1749.
1376
1377 Roach, L.H., Mustard, J.F., Lane, M.D., Bishop, J.L., and Murchie, S.L. (2010) Diagenetic
1378 haematite and sulfate assemblages in Valles Marineris. *Icarus* 207:659-674.
1379

1380 Rodgers, K.A., Cook, K.L., Browne, P.R.L., and Campbell, K.A. (2002). The mineralogy,
1381 texture and significance of silica derived from alteration by steam condensate in three New
1382 Zealand geothermal fields. *Clay Minerals* 37:299–322.
1383
1384 Rodgers, K.A., Browne, P.R.L., Buddle, T.F., Cook, K.L., Greatrex, R.A., Hampton, W.A.,
1385 Herdianita, N.R., Holland, G.R., Lynne, B.Y., Martin, R., Newton, Z., Pastars, D., Sannazarro,
1386 K.L., and Teece, C.I.A. (2004) Silica phases in sinters and residues from geothermal fields of
1387 New Zealand. *Earth Science Reviews* 66:1-61.
1388
1389 Ruff, S.W., Farmer, J.D., Calvin, W.M., Herkenhoff, K.E., Johnson, J.R., Morris, R.V., Rice,
1390 M.S., Arvidson, R.E., Bell, J.F. III, Christensen, P.R., and Squyres, S.W. (2011). Characteristics,
1391 distribution, origin, and significance of opaline silica observed by the Spirit rover in Gusev
1392 crater, Mars. *Journal of Geophysical Research* 116:E00F23.
1393
1394 Ruff, S.W., and Farmer, J.D. (2016). Silica deposits on Mars with features resembling hot spring
1395 biosignatures at El Tatio in Chile. *Nature Communications* 7:13554.
1396
1397 Ruff, S.W., Campbell, K.A., Van Kranendonk, M., Rice, M.S., Farmer, J.D. (2020). The case for
1398 ancient hot springs in Gusev Crater, Mars. Astrobiology 20: 475-499.
1399
1400 Saemundsson, K. (1991). The geology of the Krafla system. In: Nattura Myvatns, ed. Arnpor
1401 Gardarsson and Arni Einarsson. HIN, 24-95.
1402

1403 Saemundsson, K., Hjartarson, A., Kaldal, I., Sigurgeirsson, M.A., Kristinsson, S.G., and
1404 Vikingsson, S. (2012) Geological Map of the northern Volcanic Zone, Iceland. Northern Part.
1405 1:100,000. Reykjavik: Iceland GeoSurvey and Landsvierkjun.
1406
1407 Schmidt, M.E., Ruff, S.W., McCoy, T.J., Farrand, W.H., Johnson, J.R., Gellert, R., ... and
1408 Schroeder, C. (2008). Hydrothermal origin of halogens at Home Plate, Gusev crater. *Journal of*
1409 *Geophysical Research: Planets*, 113(E6).
1410
1411 Schmidt, M.E., Farrand, W.H., Johnson, J.R., Schröder, C., Hurowitz, J.A., McCoy, T.J., ... and
1412 Ming, D.W. (2009). Spectral, mineralogical, and geochemical variations across Home Plate,
1413 Gusev Crater, Mars indicate high and low temperature alteration. *Earth and Planetary Science*
1414 *Letters* 281(3-4), 258-266.
1415
1416 Schulze-Makuch, D., Dohm, J.M., Fan, C., Fairén, A.G., Rodriguez, J.A.P., Baker, V.R., and
1417 Fink, W. (2007) Exploration of hydrothermal targets on Mars. *Icarus* 189:308-324.
1418
1419 Schwenzer, S.P. and Kring, D.A. (2013). Alteration minerals in impact-generated hydrothermal
1420 systems–Exploring host rock variability. *Icarus* 226(1), 487-496.
1421
1422 Skok, J. R., Mustard, J. F., Ehlmann, B. L., Milliken, R. E., & Murchie, S. L. (2010). Silica
1423 deposits in the Nili Patera caldera on the Syrtis Major volcanic complex on Mars. *Nature*
1424 *Geoscience*, *3*(12), 838.
1425

1426 Squyres, S.W., Arvidson, R.E., Ruff, S., Gellert, R., Morris, R.V., Ming, D.W., Crumpler, L.,
1427 Farmer, J.D., Des Marais, D.J., and Yen, A. (2008) Detection of silica-rich deposits on Mars.
1428 *Science* 320:1063–1067.
1429
1430 Stefansson, V. (1981). The Krafla geothermal field, north-east Iceland. In: L. Rybach and L.J.P.
1431 Muffler (eds) Geothermal Systems: Principles and Case Histories. Wiley, New York, N.Y. 273-
1432 294.
1433
1434 Stoffregen, R.E., Alpers, C.N., and Jambor, J.L. (2000) Alunite-jarosite crystallography,
1435 thermodynamics, and geochronology, in Sulfate Minerals: Crystallography, Geochemistry, and
1436 Environmental Significance, Rev. Mineral. Geochem, edited by C. N. Alpers et al., pp. 453-479,
1437 Mineral. Soc. Amer., Washington, D. C.
1438
1439 Stoiber, R.E., and Rose, W.I. (1974) Fumarole incrustations at active Central American
1440 volcanoes. *Geochimica et Cosmochimica Acta* 38:495-516.
1441
1442 Story, S., Bowen, B.B., Benison, K.C., and Schulze, D.G. (2010) Authigenic phyllosilicates in
1443 modern acid saline lake sediments and implications for Mars. *Journal of Geophysical Research*
1444 115:E12012.
1445
1446 Thollot, P., Mangold, N., Ansan, V., Le Mouélic, S., Milliken, R.E., Bishop, J.L., Weitz, C.M.,
1447 Roach, L.H., Mustard, J.F., and Murchie, S.L. (2012) Most Mars minerals in a nutshell: Various

alteration phases formed in a single environment in Noctis Labyrinthus. *Journal of Geophysical Research* 117:E00J06.

Tosca, N.J., McLennan, S.M., Hindsley, D.H., and Schoonen, M.A.A. (2004) Acid-sulfate weathering of synthetic Martian basalt; the acid fog model revisited. *Journal of Geophysical Research* 109:E05003.

Tosca, N.J., McLennan, S.M., Clark, B.C., Grotzinger, J.P., Hurowitz, J.A., Knoll, A.H., Schröder, C., and Squyres, S.W. (2005) Geochemical modeling of evaporation processes on Mars: Insight from the sedimentary record at Meridiani Planum. *Earth and Planetary Science Letters* 240:122-148.

Velde, B. (Ed.) (1995). Origin and Mineralogy of Clays, Springs, New York.

Viviano, C.E., Moersch, J.E., and McSween, H.Y. (2013). Implications for early hydrothermal environments on Mars through the spectral evidence for carbonation and chloritization reactions in the Nili Fossae region. *Journal of Geophysical Research* 118:1858-1872.

Walter, M.R., and Des Marais, D.J. (1993). Preservation of biological information in thermal spring deposits: developing a strategy for the search for fossil life on Mars. *Icarus* 101:129-143.

Wang, A., Bell, J.F. III, Li, R., Johnson, J.R., Farrand, W.H., Cloutis, E.A., Arvidson, R.E., Crumpler, L., Squyres, S.W., and McLennan, S.M. (2008) Light-toned salty soils and coexisting

1471 Si-rich species discovered by the Mars Exploration Rover Spirit in Columbia Hills. *Journal of*

1472 *Geophysical Research* 113:E12S40.

1473

1474 Yen, A.S., Morris, R.V., Clark, B.C., Gellert, R., Knudson, A.T., Squyres, S., Mittlefehldt, D.W.,

1475 Ming, D.W., Arvidson, R., McCoy, T., Schmidt, M., Hurowitz, J., Li, R., and Johnson, J.R.

1476 (2008) Hydrothermal processes at Gusev Crater: An evaluation of Paso Robles class soils.

1477 *Journal of Geophysical Research* 113:E06S10.

1478

1479

Table 1: Hverir fumarole transect sample details, and XRD-determined relative abundances of sulfur-bearing and other phases.

						Non-sulfur bearing		Sulfur-bearing	
	Type	Distance (cm)	Depth (cm)	T (°C)	Description	Abundant	Minor	Abundant	Minor
IV-13-05	precip.	0	0	97.8	elemental sulfur at fumarole vent			S	
IV-13-06	sed	30	0	66.9	Pale orange, sandy	Si, At			
IV-13-07	sed	120	5	51.5	Reddish-orange sed under top crust	Si, At	Hm		Na
IV-13-08	sed	200	0	68.5	Tan with dark orange, sandy	Si, At	Q		
IV-13-09	sed	280	5	14.4	Tan, pale orange sed.	Si, At			
IV-13-10mix	sed	550	5	17.2	Mixed sample- dark brown sandy top, sulfur and multi-colored minerals below	Si	At, Hm, Gt	S	
IV-13-10W					White component of IV-13-10	Si, At		Rh, Gyp	
IV-13-11	sed	600	0	16.3	Dark brown fine sand with some small white crystals	Si, Pl	Sm, Aug		Fc
IV-13-12	precip.	280	0	14.4	Surface white above sample 9	Si, At			
IV-13-13	sed	550	0	17.2	Surface dark red/black above sample 10	Si, Hm	Gt		
IV-13-13PAB	rock					Si, Hm	Gt	J	
IV-13-14MIX	rock	500	0		Purple altered basalt near surface	Si	At, Hm	Mi	J
IV-13-14-W+P	rock					Si, Hm	Q, At	Mi	
IV-13-15	rock				Unaltered substrate basalt	Pl, Aug			
Hverir fumarole pits									
Pit 1									
IV-14-06	precip.	200	16	73.2	white, fibrous crystals coating lava rocks	Si, OA, Ct	At		
IV-14-07	sed	200	26	76.2	red layer with pieces of altered basalt		Si, Hm, At		
IV-14-08	sed	200	38	76.8	Massive yellow material	Si, Ct	At		
IV-14-09	sed	200	38	71.3	Purple lens	Si, Ct, Hm	At	Na	
IV-14-10	sed	200	68	69.6	White, gummy material below sample 9.	Si, Ct	At		Na
IV-14-11	rock	200	0	47.7	Chunks of altered basalt	Si, Ct	At, Hm		
IV-14-12	sed	200	18	69.6	Orange, muddy soft material	Ct, Gt	Si, At, Hm		
Pit 2									
IV-14-13	precip.	400	60	38.1	Yellowish altered soil (uniform with depth)	Si, At			
Pit 3									
IV-14-14	sed	600	30	20.6	Orange lenses (mined from yellow matrix)		Si, At, Gt	Nj	Na
IV-14-15	sed	600	50	40.5	Yellow matrix material.	Si	At		
IV-14-16 PAB	rock	600	40		Altered basalt pieces		Hm	Gyp	Na, Nj
Pit 4									
IV-14-17	sed	800	10	19.5	Orange mud layer	Ka			
IV-14-18	sed	800	15	25.1	Red mud layer	Ka	Hm	Na	
IV-14-19	sed	800	65	39.3	Light yellow/white/purple material	Si, At		S	
Pit 5									
IV-14-20	sed	0	40	97.0	White and beige mud (under sulfur crystals)	Si, At	Gt		

Phases: At= anatase, Aug = augite, Ct = cristobalite, Fc = ferricopiapite, Gt = goethite, Gyp = gypsum, Hm = hematite, J = jarosite, Ka = kaolinite, Mi = minamiite, Na = natroalunite, Nj = natrojarosite, OA = opal-A, Pl = plagioclase, Q = quartz, Rh = rhomboclase, S = sulfur, Si = amorphous silica, Sm = smectite

This is the peer-reviewed, final accepted version for American Mineralogist, published by the Mineralogical Society of America.
The published version is subject to change. Cite as Authors (Year) Title. American Mineralogist, in press.
DOI: https://doi.org/10.2138/am-2022-8363. http://www.minsocam.org/

Table 4: Major element compositions for Námafjall and other select basalts, compared to Mars

Oxide (wt. %)	1724-29 Eruption	> 6100 ka Eruption IV-13-15	Hyaloclastite IV-14-36	Mauna Kea[a]	Cerro Negro[b]	OCBP-1[c]	Adirondack[d]
SiO_2	48.80	48.77	49.27	48.70	48.40	48.19	45.30
Al_2O_3	12.70	13.13	13.43	1.40	17.70	8.06	10.40
Fe_2O_3T	15.80	15.42	14.09	12.00	9.90	20.23	21.10
MnO	0.18	0.23	0.16	0.21	0.20	0.43	0.42
MgO	5.70	6.13	5.24	3.90	6.70	10.40	11.90
CaO	10.10	10.59	10.60	6.60	11.90	6.46	7.80
Na_2O	2.30	2.14	2.20	4.30	2.00	2.19	2.10
K_2O	0.34	0.29	0.27	1.90	0.40	0.75	0.03
TiO_2	2.00	1.82	2.19	2.80	0.70	1.01	0.49
P_2O_5	0.22	0.18	0.23	0.85	0.09	1.37	0.54
SO_4	0.12	0.11	0.18	0.09	0.09	-	-
LOI	0.25	-0.62	0.62	1.60	-	-	-
Total	98.15	98.79	98.39	99.83	99.90	97.38	99.81

Bulk compositions of Icelandic basalts determined by XRF, this study.

[a]Mauna Kea (Morris et al., 2005), [b]Cerro Negro (Hynek et al., 2013).

[c]OCBP1 (Meridiani) (Morris et al., 2006), [d]Adirondack (McSween et al, 2006).

Total Fe reported as Fe_2O_3. "-" = not reported. LOI = loss on ignition, where applicable.

This is the peer-reviewed, final accepted version for American Mineralogist, published by the Mineralogical Society of America.
The published version is subject to change. Cite as Authors (Year) Title. American Mineralogist, in press.
DOI: https://doi.org/10.2138/am-2022-8363. http://www.minsocam.org/

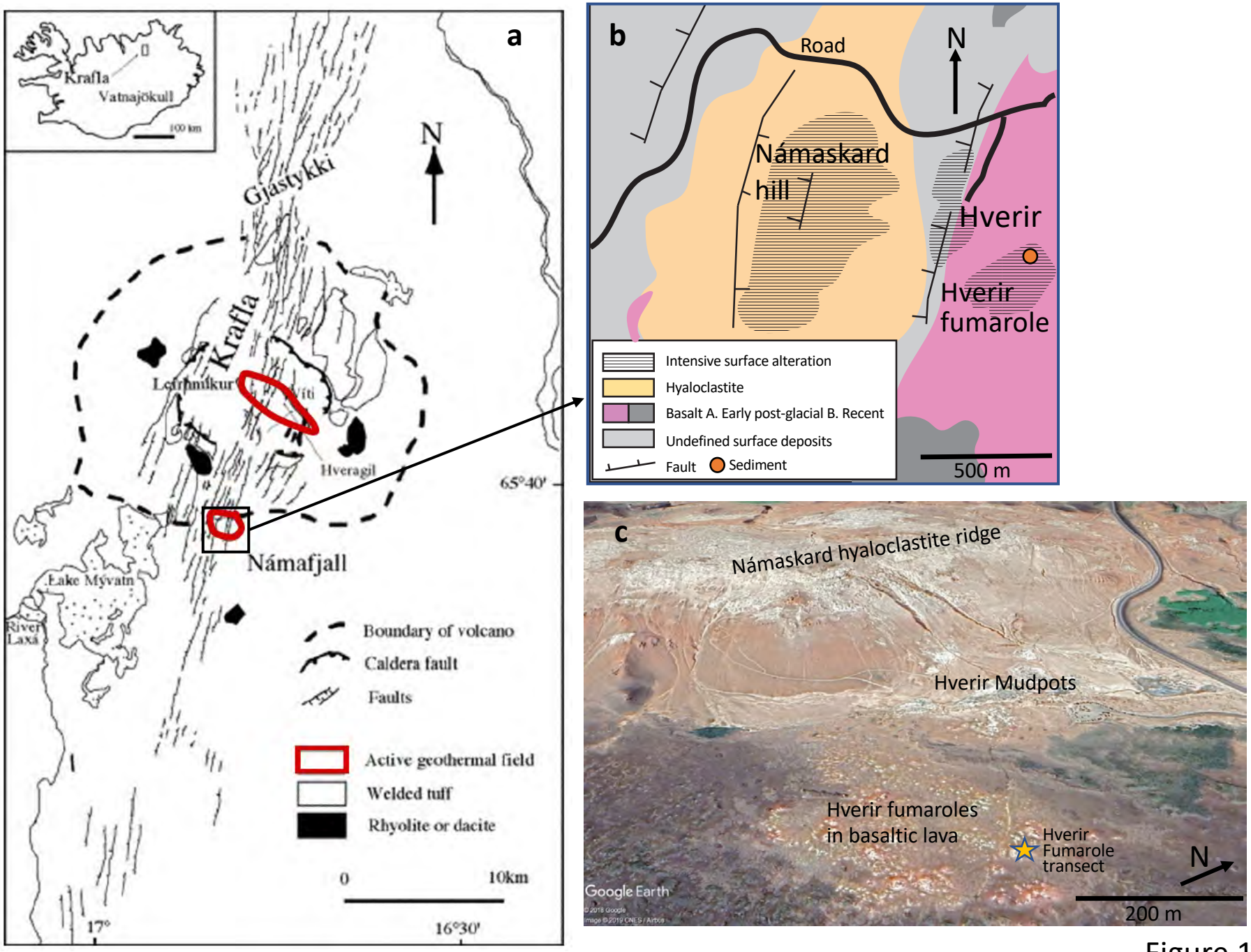

Figure 1

This is the peer-reviewed, final accepted version for American Mineralogist, published by the Mineralogical Society of America.
The published version is subject to change. Cite as Authors (Year) Title. American Mineralogist, in press.
DOI: https://doi.org/10.2138/am-2022-8363. http://www.minsocam.org/

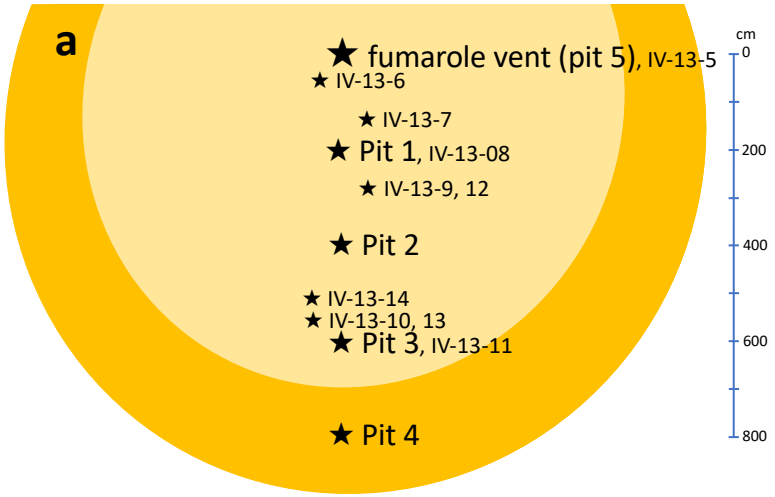

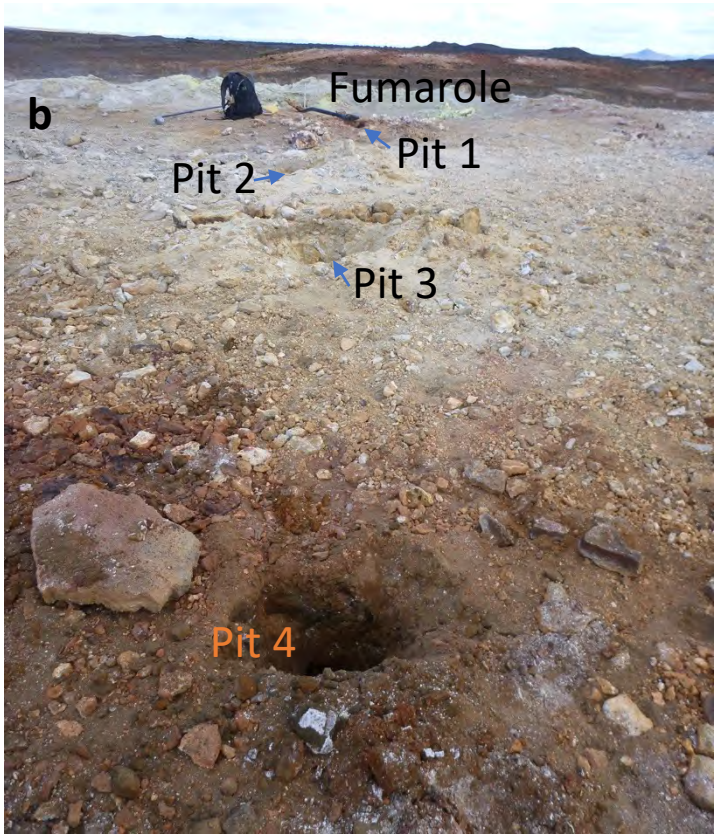

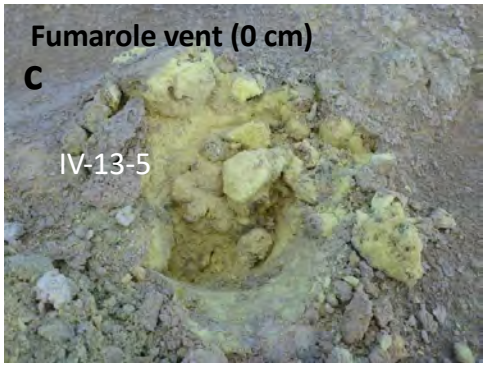

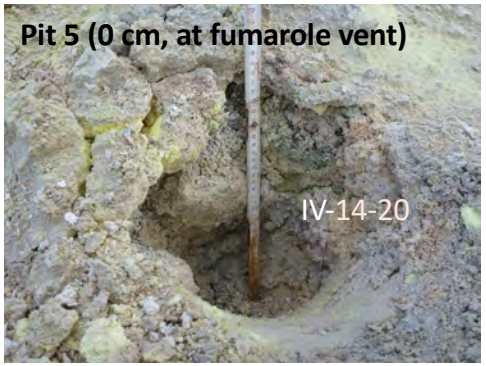

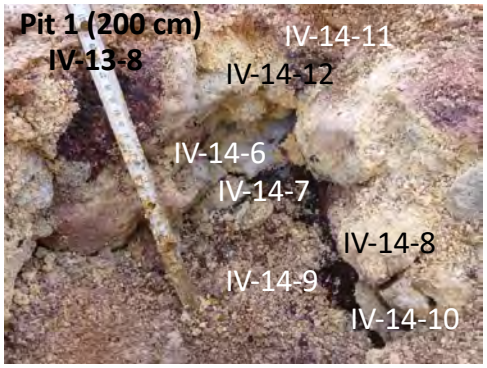

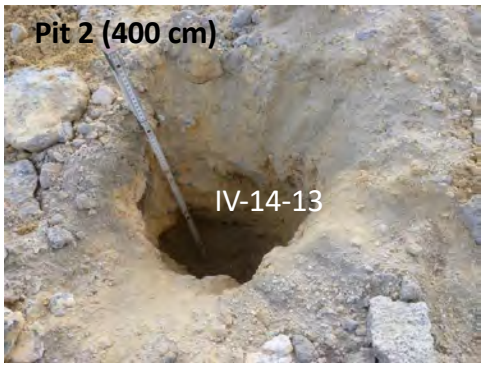

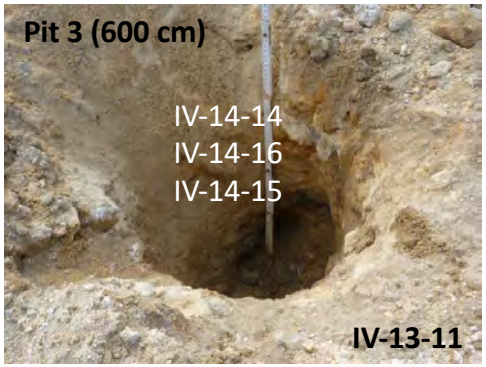

Figure 2

This is the peer-reviewed, final accepted version for American Mineralogist, published by the Mineralogical Society of America.
The published version is subject to change. Cite as Authors (Year) Title. American Mineralogist, in press.
DOI: https://doi.org/10.2138/am-2022-8363. http://www.minsocam.org/

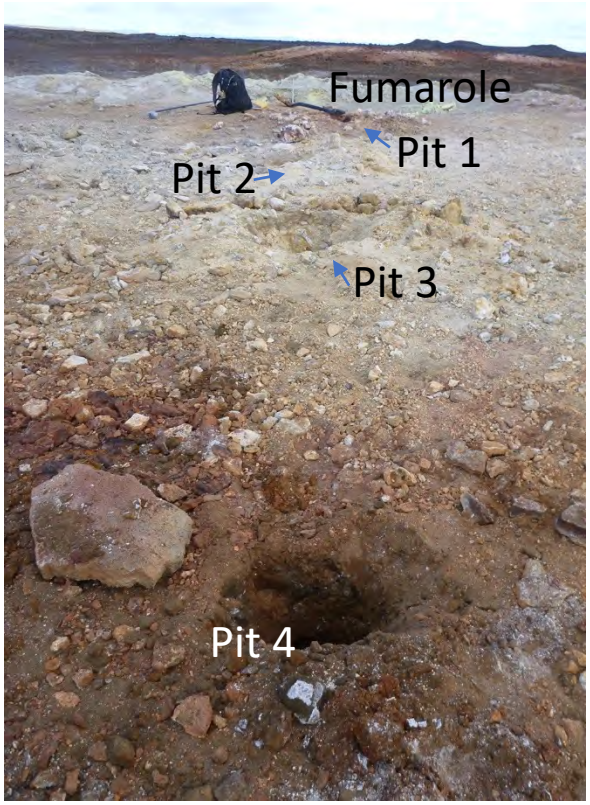

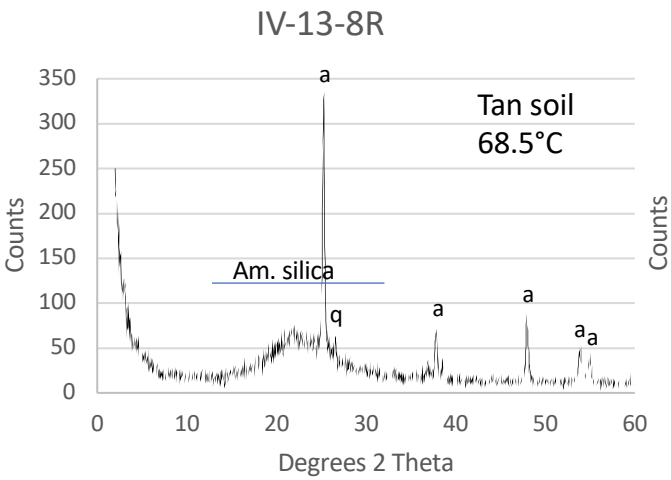

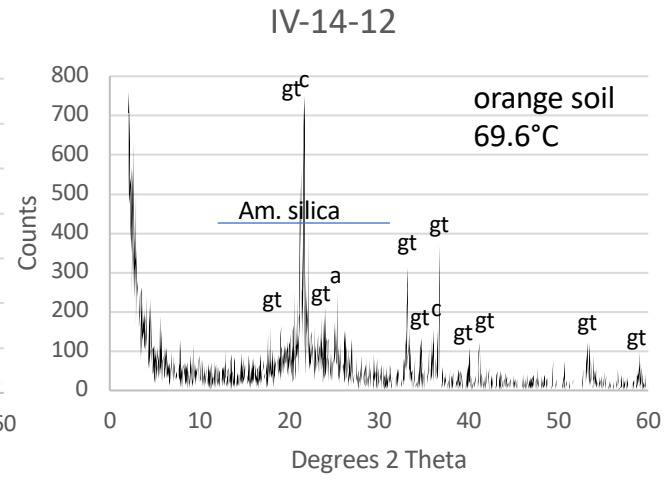

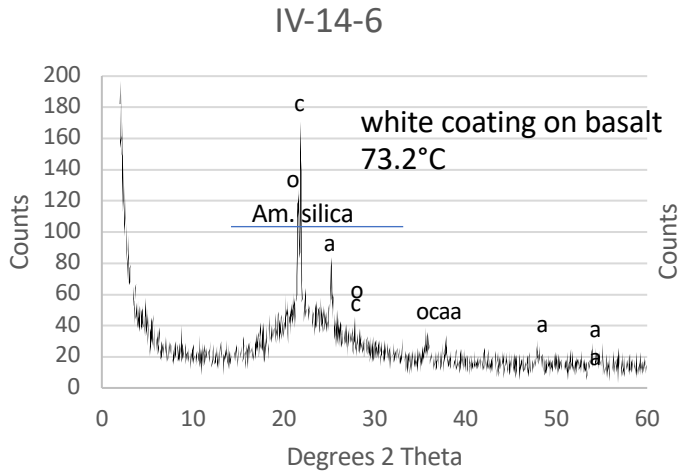

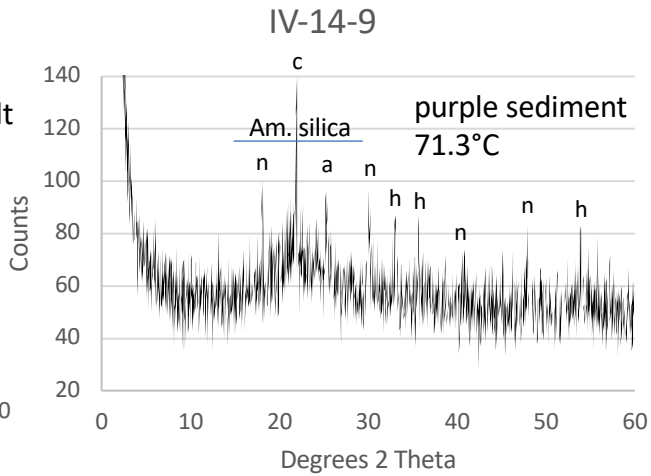

a = anatase
c = cristobalite
o = opal A
q = quartz

gt = goethite
n = natroalunite
h = hematite

Figure 3

This is the peer-reviewed, final accepted version for American Mineralogist, published by the Mineralogical Society of America.
The published version is subject to change. Cite as Authors (Year) Title. American Mineralogist, in press.
DOI: https://doi.org/10.2138/am-2022-8363. http://www.minsocam.org/

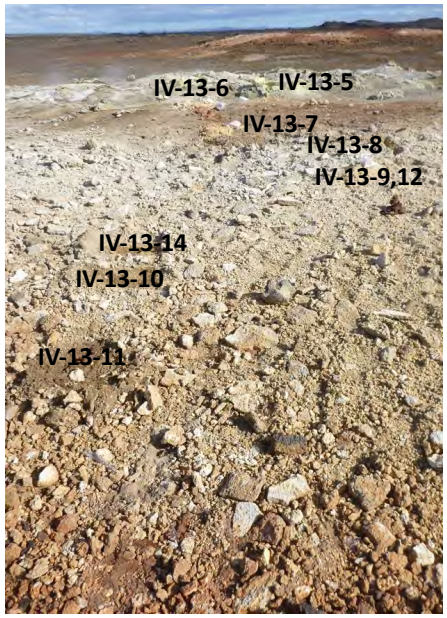

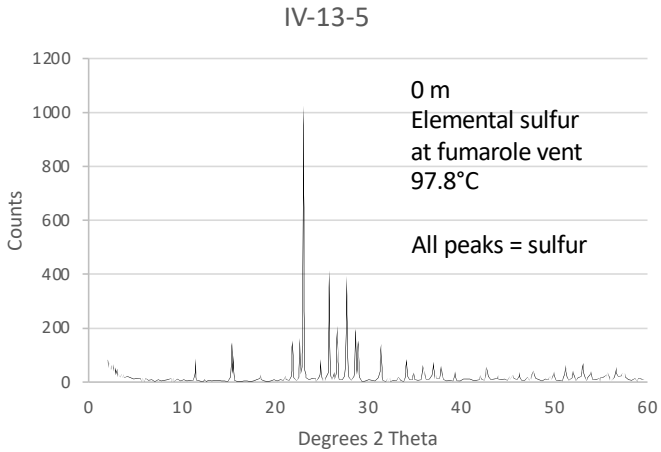

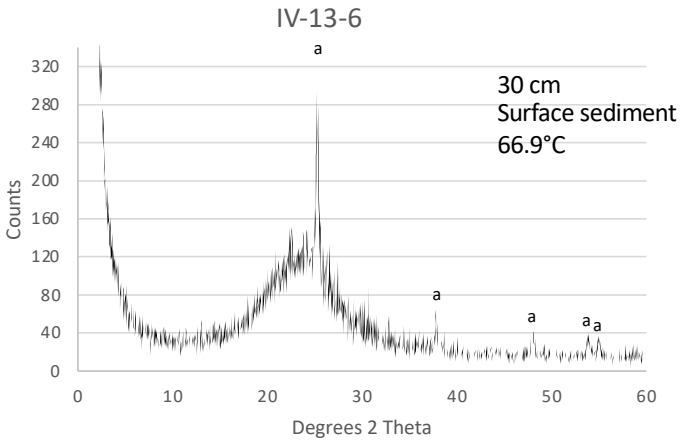

a = anatase
h = hematite
mi = minamiite
q = quartz
k = kaolinite
n = natroalunite
g = gypsum
r = rhomboclase

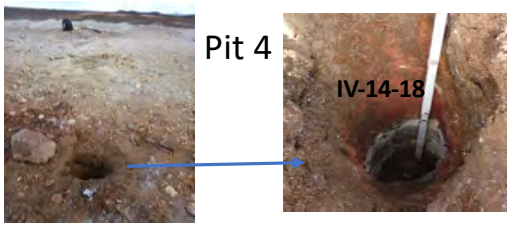

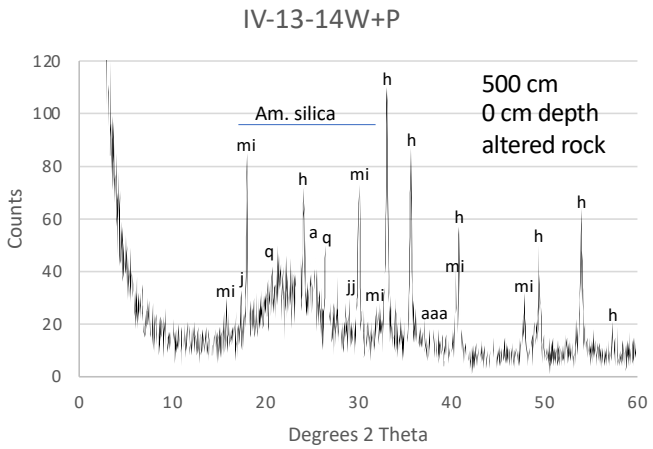

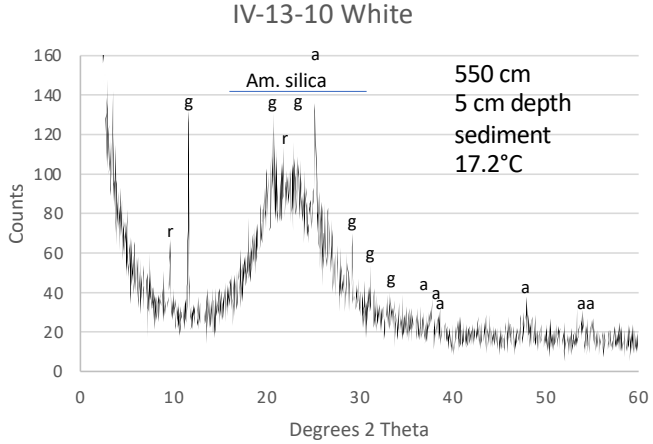

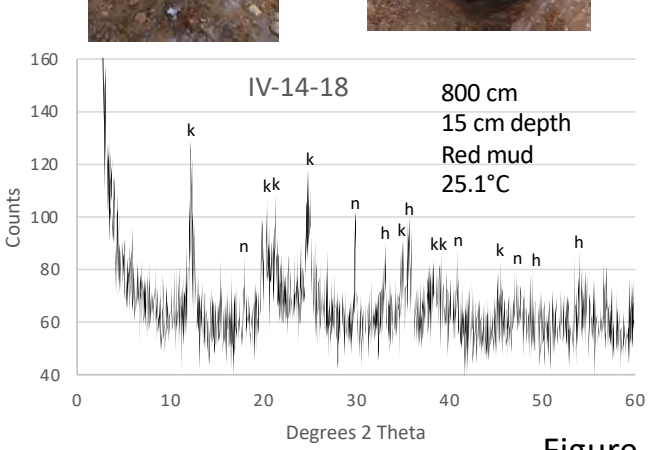

Figure 4

This is the peer-reviewed, final accepted version for American Mineralogist, published by the Mineralogical Society of America.
The published version is subject to change. Cite as Authors (Year) Title. American Mineralogist, in press.
DOI: https://doi.org/10.2138/am-2022-8363. http://www.minsocam.org/

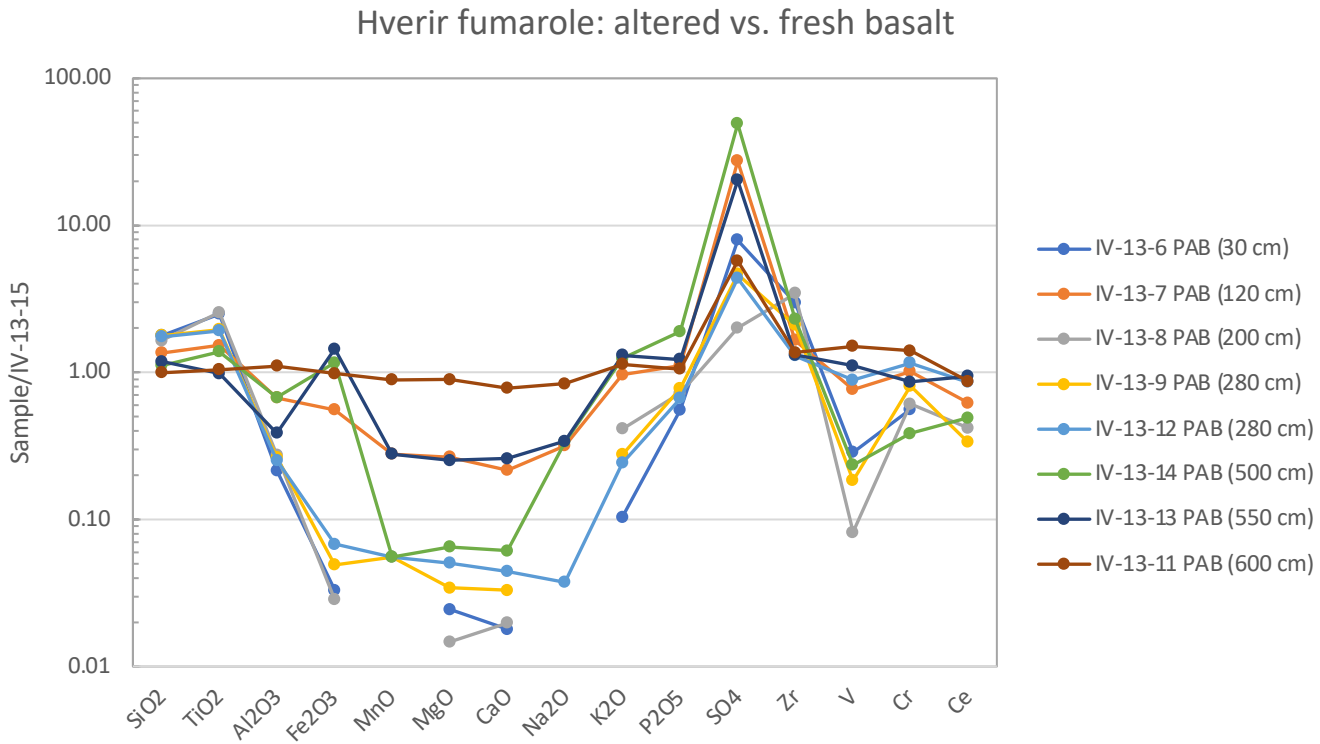

Figure 5

This is the peer-reviewed, final accepted version for American Mineralogist, published by the Mineralogical Society of America.
The published version is subject to change. Cite as Authors (Year) Title. American Mineralogist, in press.
DOI: https://doi.org/10.2138/am-2022-8363. http://www.minsocam.org/

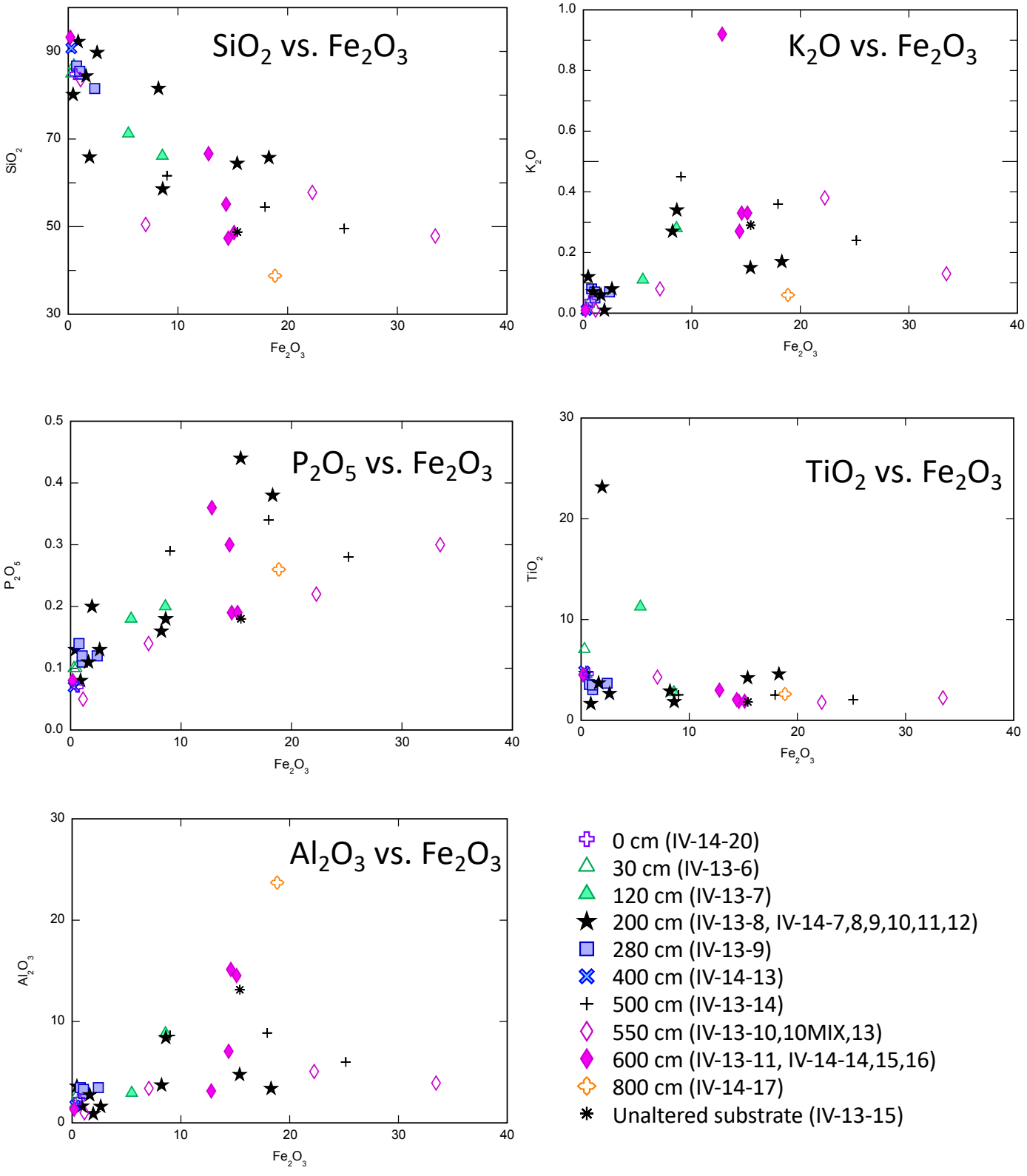

Figure 6

This is the peer-reviewed, final accepted version for American Mineralogist, published by the Mineralogical Society of America.
The published version is subject to change. Cite as Authors (Year) Title. American Mineralogist, in press.
DOI: https://doi.org/10.2138/am-2022-8363. http://www.minsocam.org/

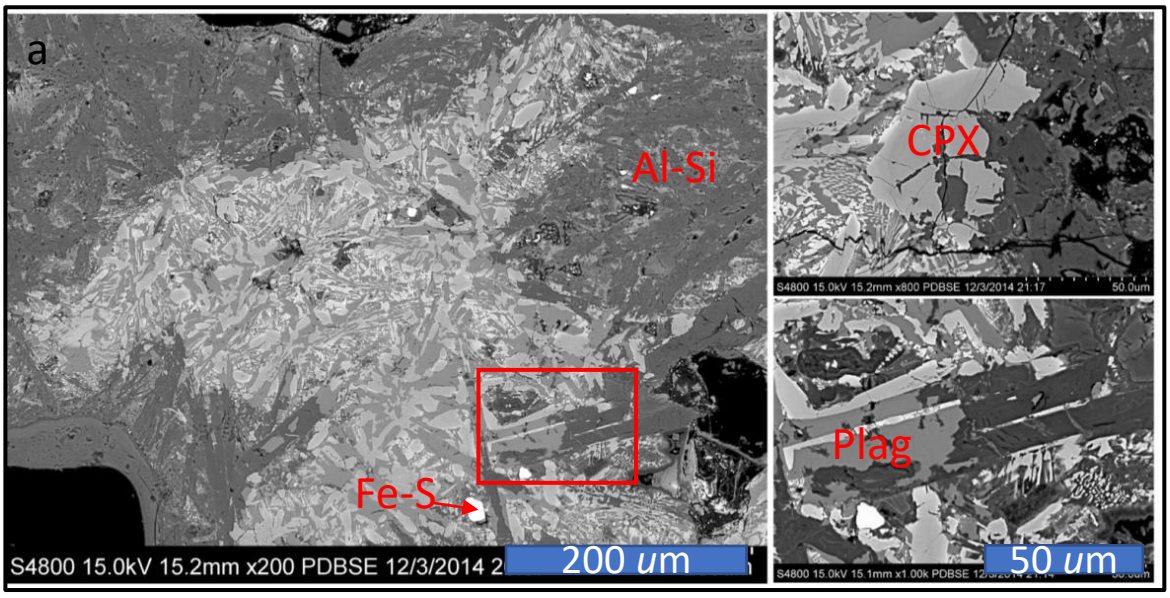

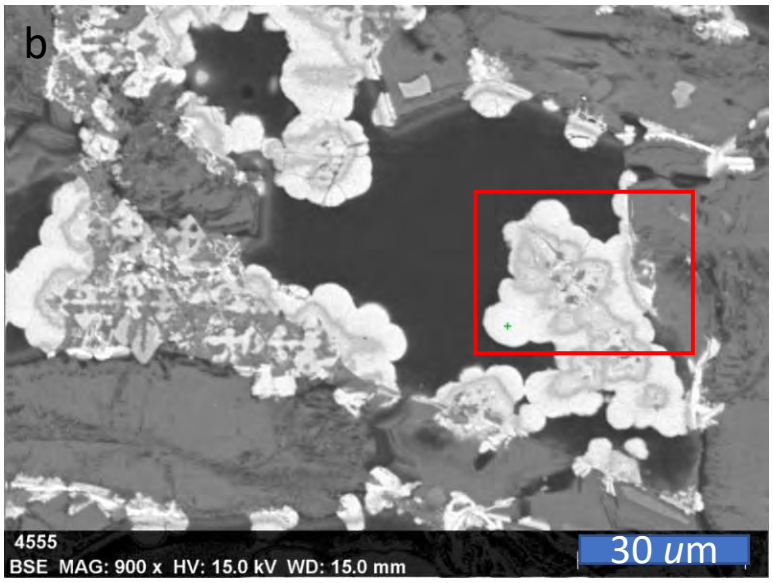

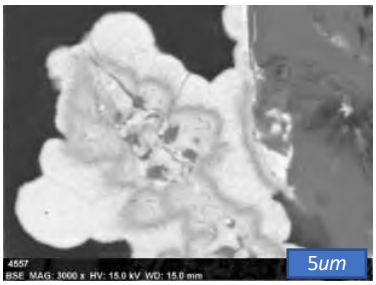

Sample IV-13-7

Figure 7

This is the peer-reviewed, final accepted version for American Mineralogist, published by the Mineralogical Society of America.
The published version is subject to change. Cite as Authors (Year) Title. American Mineralogist, in press.
DOI: https://doi.org/10.2138/am-2022-8363. http://www.minsocam.org/

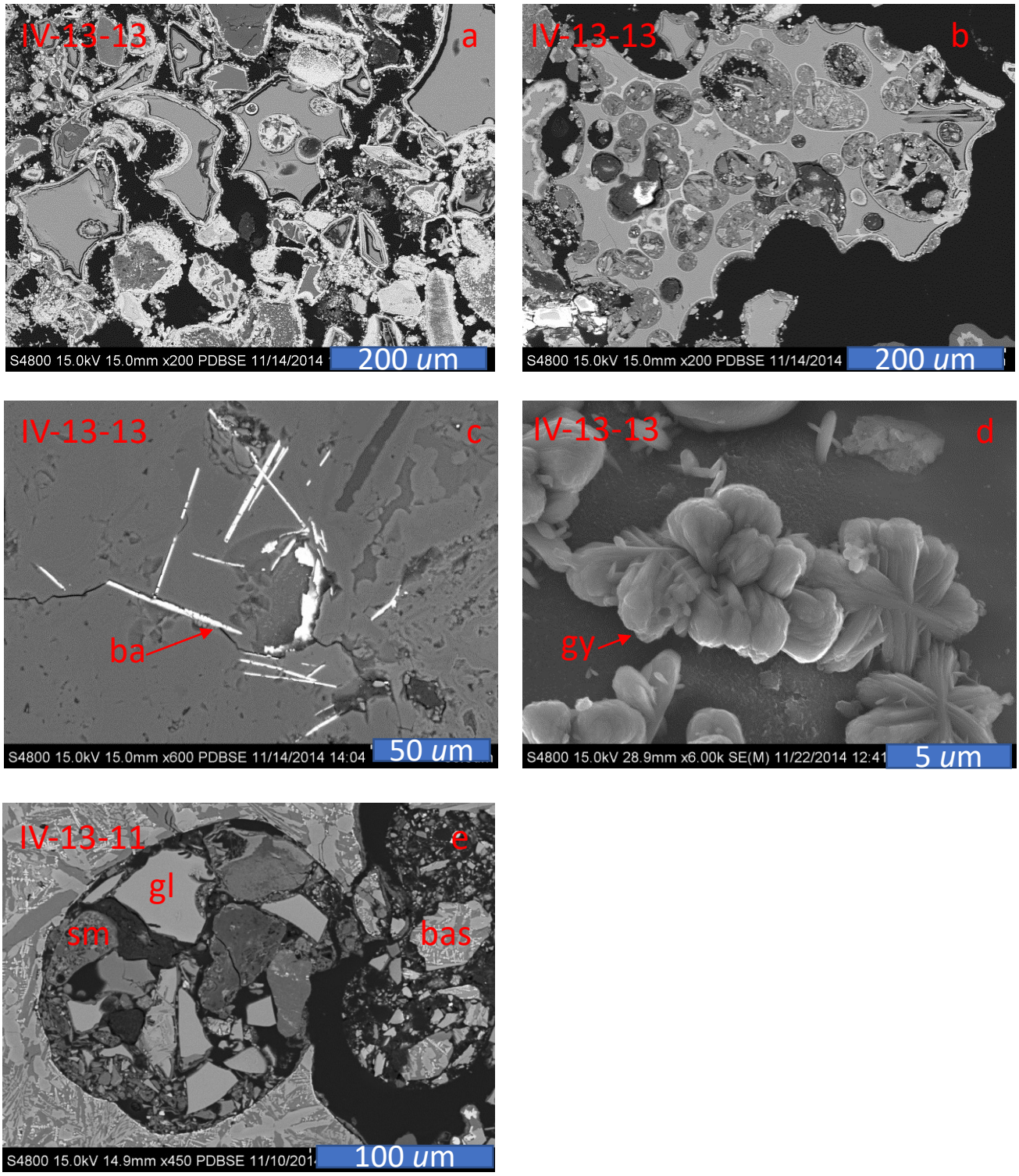

Figure 8

This is the peer-reviewed, final accepted version for American Mineralogist, published by the Mineralogical Society of America.
The published version is subject to change. Cite as Authors (Year) Title. American Mineralogist, in press.
DOI: https://doi.org/10.2138/am-2022-8363. http://www.minsocam.org/

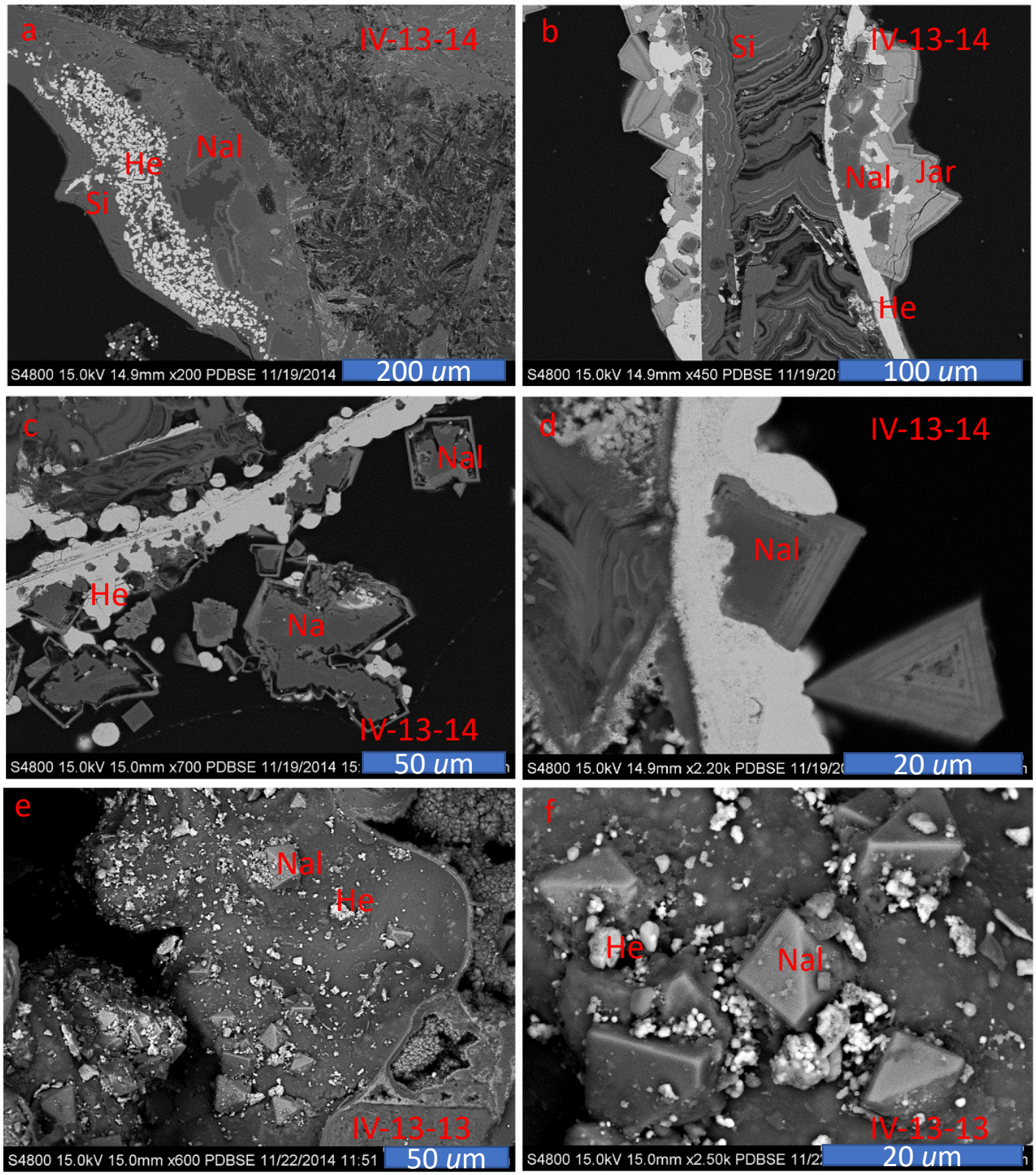

Figure 9

This is the peer-reviewed, final accepted version for American Mineralogist, published by the Mineralogical Society of America.
The published version is subject to change. Cite as Authors (Year) Title. American Mineralogist, in press.
DOI: https://doi.org/10.2138/am-2022-8363. http://www.minsocam.org/

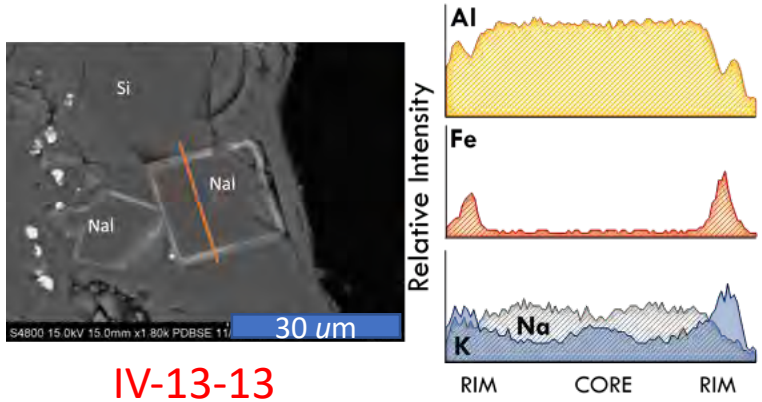

IV-13-13

Figure 10

This is the peer-reviewed, final accepted version for American Mineralogist, published by the Mineralogical Society of America.
The published version is subject to change. Cite as Authors (Year) Title. American Mineralogist, in press.
DOI: https://doi.org/10.2138/am-2022-8363. http://www.minsocam.org/

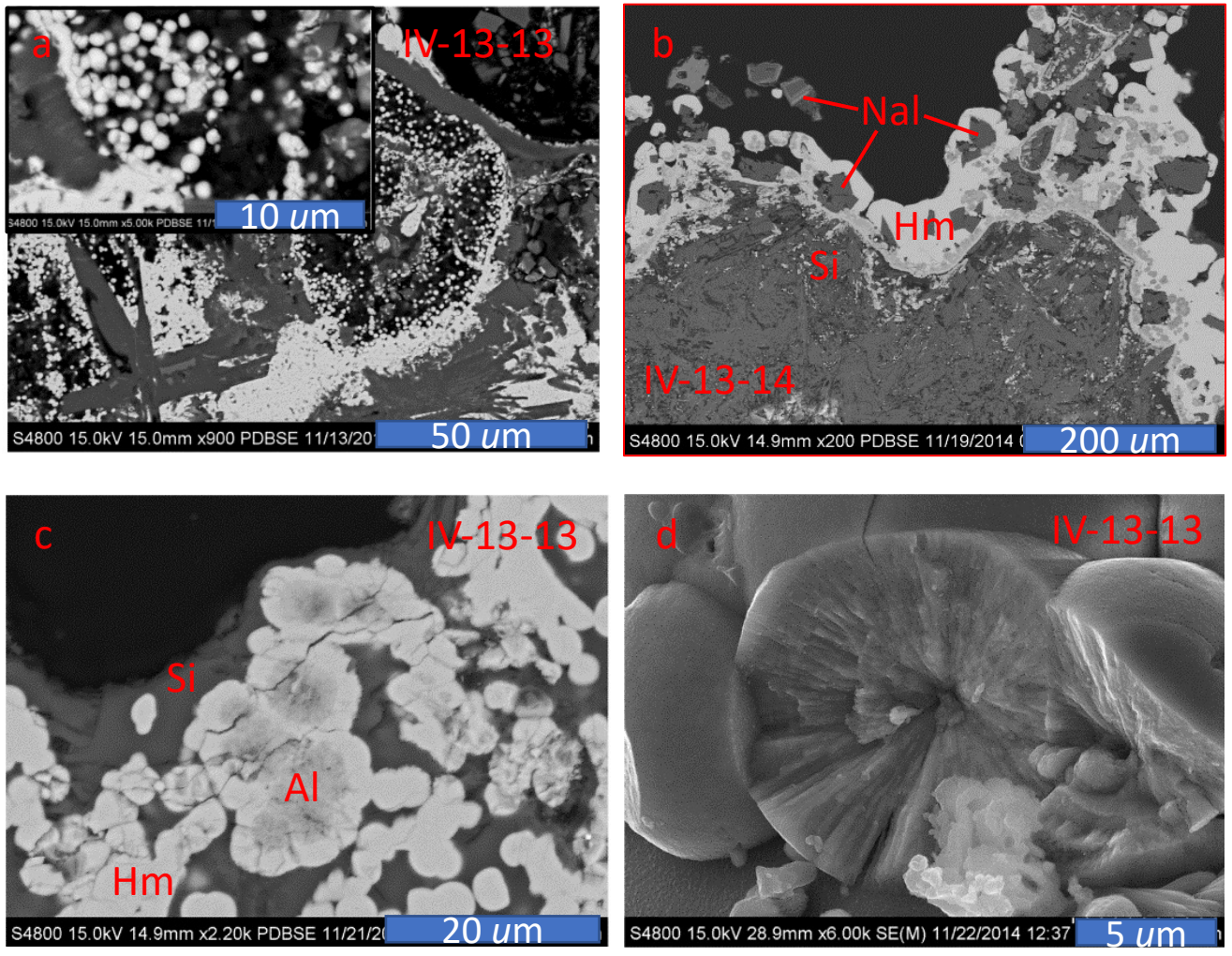

Figure 11

This is the peer-reviewed, final accepted version for American Mineralogist, published by the Mineralogical Society of America.
The published version is subject to change. Cite as Authors (Year) Title. American Mineralogist, in press.
DOI: https://doi.org/10.2138/am-2022-8363. http://www.minsocam.org/

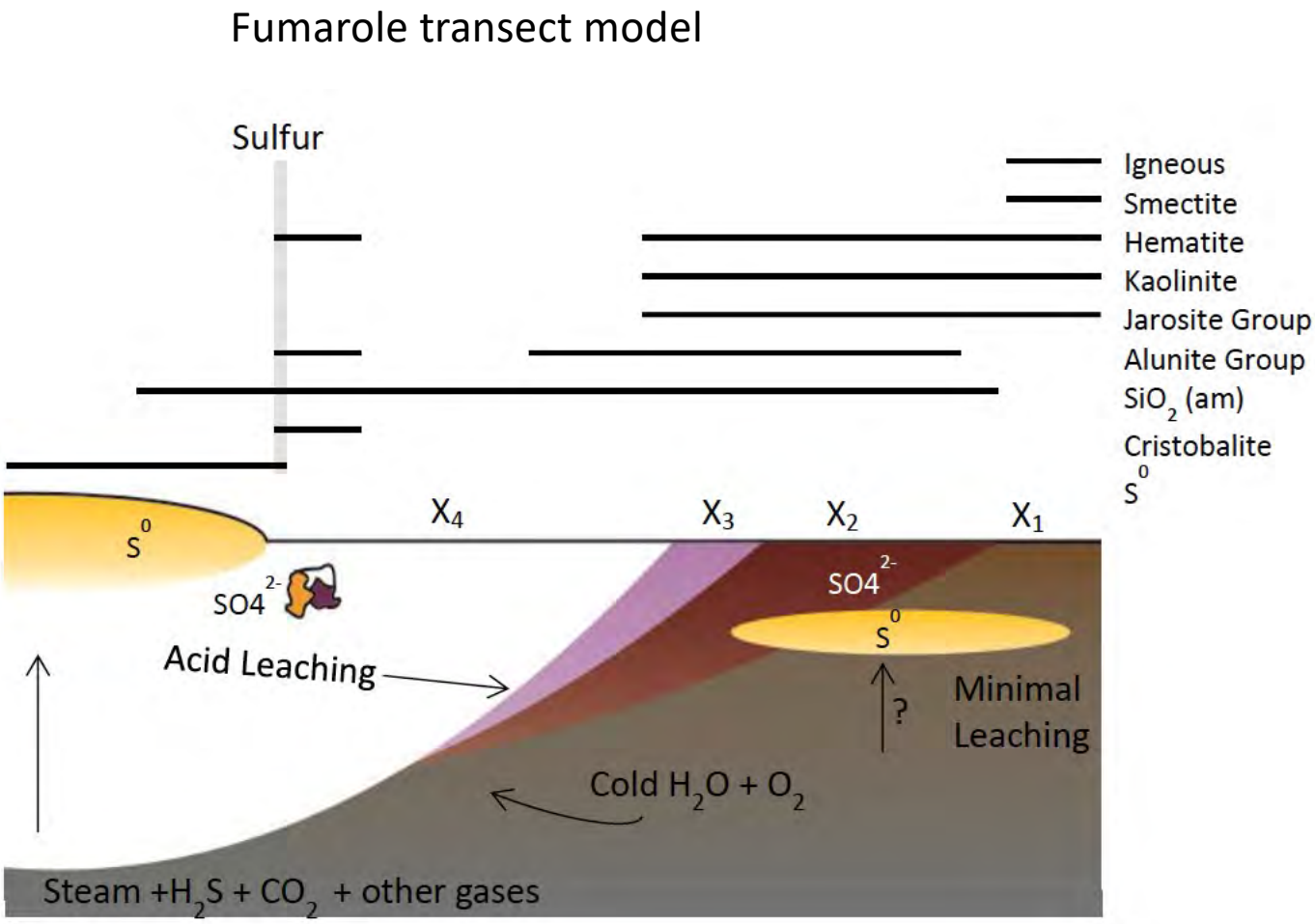

Figure 12

This is the peer-reviewed, final accepted version for American Mineralogist, published by the Mineralogical Society of America.
The published version is subject to change. Cite as Authors (Year) Title. American Mineralogist, in press.
DOI: https://doi.org/10.2138/am-2022-8363. http://www.minsocam.org/

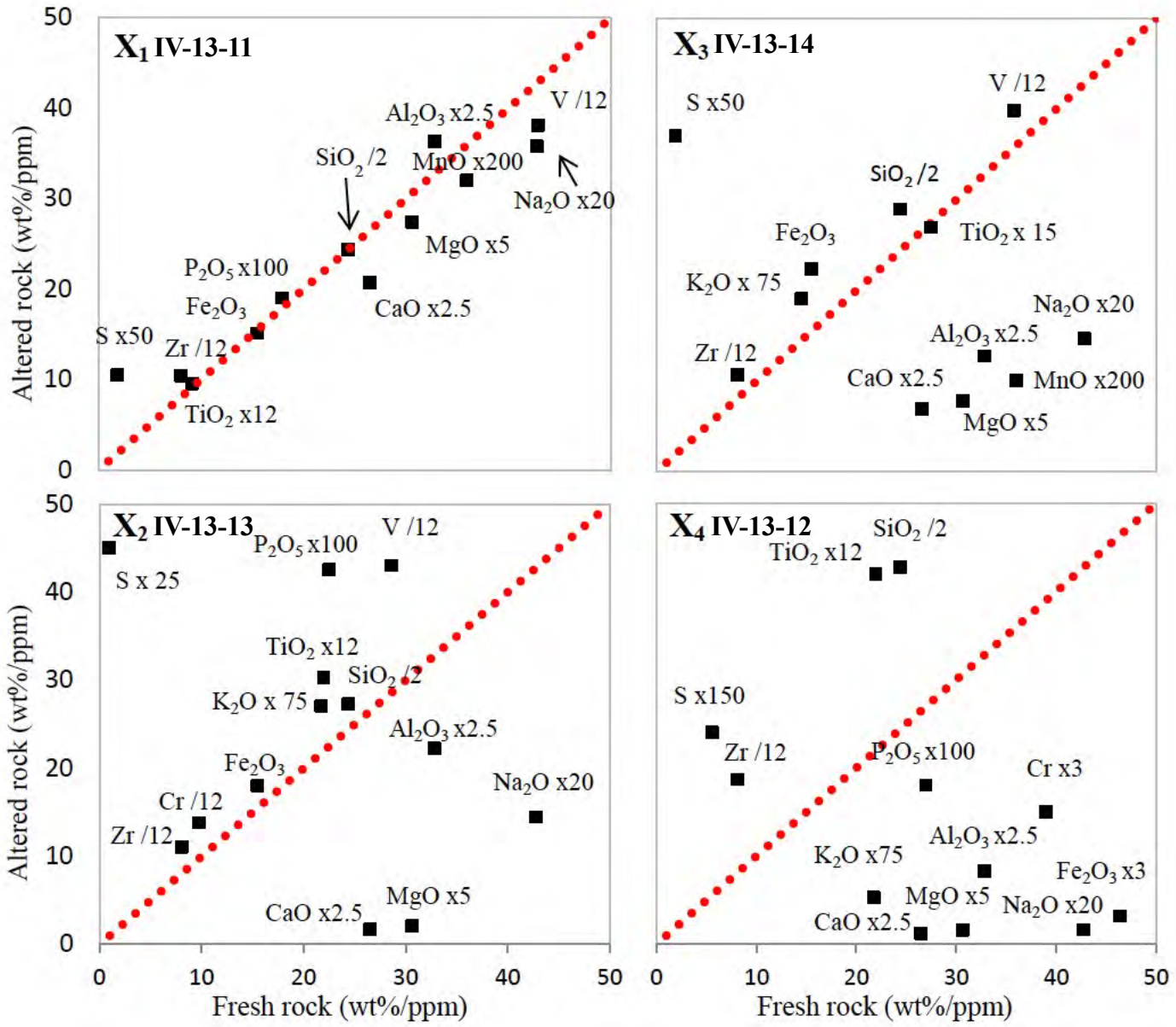

Figure 13